



Intermetallic based materials for Sabatier reaction: Surface understanding, performance assessment and comparison with commercial catalyst

Riccardo Freccero^{a,b}, Elena Spennati^{b,c}, Gabriella Garbarino^{b,c,*}, Paola Riani^{a,b,**}

^a Department of Chemistry and Industrial Chemistry, University of Genova, Via Dodecaneso 31, 16146 Genova, Italy

^b INSTM, UdR di Genova, Via Dodecaneso 31, 16146 Genova, Italy

^c Department of Civil, Chemical and Environmental Engineering, University of Genova, Via all'Opera Pia 15, 16145 Genova, Italy

ARTICLE INFO

Keywords:

RENi₅
CO₂ hydrogenation
Synthetic natural gas
Intermetallics
Surface simulation

ABSTRACT

Ni-based intermetallics and commercial CO₂ hydrogenation catalysts have been compared in Sabatier's reaction. For RENi₅ intermetallics (RE = La, Ce), the analysis of the chemical bonding shows a charge transfer from the RE to the Ni species and the formation of polar two- and four-atomic RE-Ni and four-atomic Ni bonds. Surface simulations and chemical understanding based on the ELI-D mapping approach indicate that dangling bonds originate from the multi-atomic ones and they are the preferred adsorption sites for H₂ molecules. This leads to H₂ dissociation, its reduction to hydrides, Ni QTAIM-anion oxidation to the metallic state, and diffusion toward the surface. LaNi₅ is active toward rWGS while the best catalytic activity is obtained over CeNi₅ (49% methane yield) at 723 K; the exhaust catalyst is composed of Ni particles supported over CeO₂ with a mean size of 10 nm and thus, promising material could be developed on intermetallic based compounds.

1. Introduction

The large quantities of CO₂ emitted into the atmosphere represent one of the most relevant environmental problems of modern days. In 2021, the total anthropogenic fossil CO₂ emissions, around 39.7 Gton, increased by 5.3% in comparison with 2020 ones [1]. To achieve the 2030 climate target plan set by the European Commission, consisting of greenhouse gas emissions reduction by at least 55% by 2030, and COP26 (November 2022) goals of ensuring the global net zero by mid-century and keeping the temperature of 1.5 K above preindustrial levels, new strategies and processes for the CO₂ utilization need to be found [2]. The CO₂ conversion to methane by using green hydrogen is considered a promising process that reduces CO₂ emissions and exploits its possible uses. CO₂ hydrogenation, known as the Sabatier reaction ($\text{CO}_{2(g)} + 4 \text{H}_{2(g)} \rightleftharpoons \text{CH}_{4(g)} + 2 \text{H}_2\text{O}_{(g)}$) is an exothermic reaction ($\Delta H_{298 \text{ K}}^0 = -164 \text{ kJ/mol}$) favorable at low temperature and high pressure and generally performed in between 423 and 773 K and 1–100 atm [3], in the presence of a catalyst.

Conventional catalytic materials are either Ru- or Ni-based, supported on oxides, with high surface area and good thermal stability such as $\gamma\text{-Al}_2\text{O}_3$, SiO₂, TiO₂, etc [4,5]. In patent and literature, available

formulation accounts also for the presence of promoters and dopants; active phase loading varies in between 0.5 and 3 wt% and 10–70 wt% for Ru and Ni, respectively [6]. Ni is accounted as a more promising active phase for medium temperature reaction ranges but it suffers from particle sintering, coke deposition, and limited activity at low temperatures, with even the possible production of Ni(CO)₄. For these reasons, the investigation of new catalysts formulation is increasingly attracting the attention of researchers. In a recent review, lanthanides i.e., Ce, La, Pr, Nd, and Sm, have been reported as suitable promoters but costs and the effort in reduction of critical raw material use, need to be accounted for catalyst design, taking into account the complex frame of the energy transition elements [6,7].

Another possibility, regarding CO₂ hydrogenation to methane, is to consider intermetallic compounds (IMCs) as viable alternatives to supported catalysts or as their precursors.

IMCs are defined as crystalline phases containing at least two metals, with optionally one or more non-metallic elements, whose structure is different from those of the constituting atoms in the elemental state [8]. IMCs do not follow well-established valence electron rules, due to electron deficiency, resulting in the impossibility to predict their formation with selected structures and stoichiometries.

* Corresponding author at: Department of Civil, Chemical and Environmental Engineering, University of Genova, Via all'Opera Pia 15, 16145 Genova, Italy.

** Corresponding author at: Department of Chemistry and Industrial Chemistry, University of Genova, Via Dodecaneso 31, 16146 Genova, Italy.

E-mail addresses: gabriella.garbarino@unige.it (G. Garbarino), paola.riani@unige.it (P. Riani).

Their unique and often complex crystal and electronic structures lead to unexpected and unprecedented bonding scenarios, making them prone to display exotic reactive behaviors [9,10]. Such bonding scenarios are typically precluded to common inorganic materials like oxides and substitutional alloys.

Recently, thanks to the development of new theories of chemical bonding based on DFT calculations, the electronic structure and therefore the reactivity of some IMCs has become accessible. These results inspired their chemical application as heterogeneous catalysts. It is worth noting that relevant results have already been published for several processes such as methanol steam reforming, semi-hydrogenation of acetylene, water oxidation, biomass upgrading and CO₂ valorization [9–13]. Among them, Al₁₃Fe₄ [14], GaPd, and GaPd₂ tested in the semi-hydrogenation of acetylene and methanol synthesis [15], and Cu/Pd-Zr intermetallics tested in methanol steam reforming are worth mentioning [16]. Such tests have been performed using both supported and unsupported IMCs. The promising results obtained in terms of activity and selectivity have been related to some features of IMCs like stability against segregation, well-defined compositional and electronic properties, versatility ensured by a wide range of accessible chemical potentials of the involved transition metal, and peculiar combination of electronic and crystal structures [17]. Moreover, Zhang et al. studied the in-situ formation of CoIn₂ IMC as a new active phase to adsorb and activate CO₂ for its hydrogenation to methanol [18], while Duyar et al. tested catalysts containing Ni₃Ga and Ni₅Ga₃ IMCs in the methanol synthesis from CO₂ at 10 atm and 473 – 543 K [19].

Among the various families of IMCs of potential interest for catalysis, and particularly in hydrogenation reactions, those capable of storing hydrogen have to be mentioned because hydrogen absorption has been reported to potentially improve catalytic activity [20]. This is the case for IMCs of the RENi₅-type (*RE* = rare earth metal) and Mg₂Ni, active in the hydrogenation of alkynes (acetylene and propyne) [21,22], ethylene [23,24], and carbon dioxide [25–27]. Anyways, to the best of our knowledge, the literature does not provide deep and numerous investigations and understandings on CO₂ hydrogenation to methane with *RE*-based IMCs. In fact, although the structure and applications of LaNi₅ based compounds have been recently reviewed by Joubert and co-workers [28], their potential use as methanation materials, and more in general as catalysts, was not mentioned. LaNi₄X-type intermetallic compounds (X = Ni, Cr, Al, and Cu) as catalyst precursors for CO₂ methanation were investigated, for the first time, by Ando et al. in 1995 [26]. The best results were obtained with LaNi₅ at 50 atm and 573 K, achieving a CO₂ conversion of 95% and 99% of CH₄ selectivity at high contact times. Yatagai et al. investigated methane production over LaNi₅ powders mechanically ball-milled in a mixture of CO₂ and H₂ gases; moreover, LaNi₅ was also activated with a hydrogen treatment at 2 MPa and 297 K in a Sievert's apparatus to obtain the LaNi₅H₆ phase, showing enhanced catalytic activity [29]. LaNi₅H₅ was also successfully tested in the same reaction; the hydride was previously prepared by reaction of LaNi₅ with H₂ and then directly employed as a hydrogen source in an autoclave under 3 MPa of mixed gas (CO₂:Ar = 19:81), at 423–493 K [30].

It is worth noting that, although some substitutions of Ni with other metals have been investigated [26], the same is not true for the lanthanides; for this reason, in this work, also CeNi₅ IMC was investigated in CO₂ methanation taking into account its negligible hydrogen adsorption capacity [31] and lacking information in the open literature, coupled with the reported promotion effect often observed for supported Ni-based catalysts [6].

To shed light on the possible application of intermetallic for CO₂ conversion, the aim of the present work is a synergistic investigation of catalytic activity and evolution of intermetallic in the reaction environment by further investigating the chemical bond in the precursor material and changes occurring by means of theoretical modeling. For this reason, a series of IMCs have been synthesized and tested and theoretical modeling has been carried out on the most promising

material as hereinafter reported. In particular, we investigated Al richest intermetallic compounds Al₁₃Fe₄, Al₉Co₂, and Al₃Ni, to compare with obtained data for Ni/Al₂O₃ system [32–34,94] and for the previous hypothesis of an enhanced activity observed when the active atom is surrounded by the inert one [10,14], according to the active-site isolation concept developed in the '70 s [35]. Moreover, considering the interest in highly loaded Ni-based catalysts for SNG and the role of lanthanides in catalyst formulation [6], LaNi₅ and CeNi₅ have been tested for CO₂ hydrogenation.

2. Material and methods

2.1. Intermetallic preparation

Samples of nominal composition Al_{77.0}Fe_{23.0} (AF), Al_{82.8}Co_{17.2} (AC), Al_{77.0}Ni_{23.0} (AN), and RE_{16.5}Ni_{83.5} (*RE* = La, Ce; LN and CN) were prepared by direct synthesis of the pure elements and tested as catalysts for the Sabatier reaction. The nominal compositions of the aluminum-containing specimens were selected to obtain small quantities of Al together with the targeted intermetallic compound as the majority phase: Al₁₃Fe₄, Al₉Co₂, and Al₃Ni, respectively. LN and CN samples were prepared with a nominal composition corresponding to the 1:5 *RE*/Ni stoichiometric ratio, aiming to synthesize LaNi₅ and CeNi₅ single-phase samples. The employed starting materials were aluminum (rod, 99.999 mass % purity, Kryal Vaw AG., Bonn, Germany), iron, cobalt, nickel (rod, 99.998 mass % purity, Newmet Kock, Waltham Abbey, UK), lanthanum and cerium (rod, 99.9 mass % purity, Newmet Kock, Waltham Abbey, UK). Ingots of about 1.500 g were prepared by arc-melting the pristine elements with a tungsten electrode on a water-cooled copper heart under an argon atmosphere. A zirconium piece was used as oxygen getter. To ensure sample homogenization, the resulting alloys were turned over and re-melted several times. Weight losses were always smaller than 0.2 wt%.

Samples were then inserted in an alumina crucible and sealed in a quartz ampoule under an argon atmosphere and annealed at temperatures selected according to the corresponding phase diagrams [36,37]. Al₁₃Fe₄, Al₃Ni and RENi₅ (*RE* = La, Ce) were annealed for one week at 1273 K, 1023 K, and 1373 K, respectively, whereas Al₉Co₂ was annealed at 848 K for 20 days, to remove residual Al₁₃Co₄. Such details, together with sample labels and nominal compositions are listed in Table 1S (in Electronic Supplementary Information).

2.2. Material Characterization

2.2.1. Chemical and morphological characterization

The microstructural characterization of fresh, pre-reduced and exhaust intermetallic catalysts was performed to obtain, for each sample, phase distribution and the corresponding qualitative and quantitative information. For this purpose, fresh materials were analysed by using a scanning electron microscope (SEM) Zeiss Evo 40 (Carl Zeiss SMT Ltd, Cambridge, England), equipped with an Energy Dispersive X-ray (EDX) Spectroscopy Oxford Instruments INCA X-ACT. The compositional analysis was performed based on the characteristic X-ray intensities of each element, compared with standards (pure elements), and corrected for ZAF effects. A Co standard was used to monitor the beam current, gain, and resolution of the spectrometer.

Pre-reduced and exhaust catalysts were investigated by means of a scanning electron microscope Zeiss SUPRA 40 VP, equipped with a field emission gun (FE-SEM). This microscope, in addition to conventional detectors for secondary and back-scattered electrons, is equipped with a high sensitivity “InLens” secondary electron detector and with an EDX Spectrometer OXFORD “INCA Energie 450 × 3”.

To be visualized and analysed by SEM-EDXS, fresh intermetallic samples were embedded in a phenolic resin with carbon filler, by using the automatic hot compression mounting press Opal 410 (ATM GmbH, Germany). The automatic grinding and polishing machine Saphir 520

(ATM GmbH, Germany) was used to obtain smooth material surfaces suitable for microscopic examinations. Grinding was performed by means of silicon carbide grinding papers with grain size decreasing from 600 to 1200 mesh, using running water as a lubricant; for polishing diamond pastes with particle size decreasing from 6 to 1 μm were used and petroleum ether was added as a lubricant.

For high magnification micrographs, both pre-reduced and exhausted catalytic powders were directly mounted on a high-purity conductive double-sided adhesive carbon tab to be visualized and analysed by means of FESEM-EDXS.

2.2.2. Crystallographic characterization

X-ray powder diffraction measurements (XRPD) were performed by means of a Philips X'Pert MPD diffractometer equipped with a $\theta - 2\theta$ Bragg-Brentano geometry (Cu K α radiation, $\lambda = 1.5406 \text{ \AA}$, graphite crystal monochromator, PIXcel^{1D} detector). Powder patterns were collected on all samples and on a LaB₆ line position and shape standard, in the $10\text{--}100^\circ 2\theta$ range, with a scanning step of 0.0131° and with an acquisition time per step of 400 s, operating in a continuous scan mode. Obtained patterns were visualized and indexed with the aid of the PowderCell software [38], and lattice parameters of the detected phases were evaluated by a least-square method as implemented in LATCON [39]. Semi-quantitative phase analysis and estimation of the crystallite sizes, particularly for tested samples, were performed using the Match! Software [40]. For this purpose, profile fittings were effectuated by optimizing peak positions, intensities, and Full Width at Half Maximum (FWHM), yielding a good agreement between the calculated and experimental powder patterns (R_p -factors always lower than 3.0%). The Reference Intensity Ratio (RIR) method was applied for the semi-quantitative phase analysis [41], whereas the average crystallite sizes were estimated with Scherrer's formula (Scherrer constant $K = 0.94$). The FWHM values were used only after subtracting the instrument contribution to the peak broadening by generating an instrumental standard fitting of the measured powder LaB₆ profile.

2.3. Computational techniques

The electronic structures of crystalline LaNi₅ and CeNi₅ were calculated at the DFT/PBE level of theory by means of the all-electron Full-Potential Local-Orbital (FPLO) code, using the experimentally determined structural parameters [42,43]. The Brillouin zone was sampled with a (12 12 12) k -point mesh. Both spin-unpolarized and spin-polarized calculations were performed, including an additional calculation with an on-site Coulomb repulsion parameter U for the Ce 4 f states; the characteristic FPLO value of 8 eV for U ($J = 0$ eV) and the atomic-limit double-counting scheme were selected [44,45]. Relativistic effects were treated in all cases at the scalar-relativistic level. The chemical bonding for LaNi₅ and CeNi₅ was investigated by applying quantum chemical techniques in position space. For this purpose, the electron density (ED) and the electron localizability indicator, in its ELI-D representation [46,47] were calculated in an equidistant grid of about 0.05 Bohr by means of an implemented module within the FPLO code [48]; both scalar fields were analysed in the framework of the Quantum Theory of Atoms In Molecules (QTAIM) with the DGrid software [49–51]. The crystal space is partitioned into atomic basins (QTAIM atoms) or chemical regions i.e., core and valence basins (ELI-D basins), bounded by the zero-flux surfaces of the ED and of the ELI-D gradient vector fields, respectively. The integration of the ED within QTAIM or ELI-D basins leads to atomic or core/valence average electronic population. Atomic effective charges (Q^{eff}) were calculated by subtracting the obtained QTAIM atomic population from the atomic number. ELI-D valence basins i.e., bonding and lone pair ones, were analysed based on the QTAIM/ELI-D intersection techniques [52], allowing to evaluate bonding polarity and atomicity (α) [53–55]. The electrons contributed by the neighbouring QTAIM atom (X) to and ELI-D

basins (B_i) is quantified by the bond fractions: $p(B_i^X) = \frac{N(B_i^X)}{N(B_i)}$ [53,54], where $N(B_i)$ is the population of a B_i ELI-D basin, and $N(B_i^X)$ is the population of the portion of the B_i ELI-D basin intersected by the X QTAIM atom. Then, a $p(B_i^X)$ equal to 1 suggests interpreting a valence ELI-D basin as a lone pair, whereas a $p(B_i^X)$ equal to 0.5 as a homopolar bond; intermediate values indicate polar covalent interactions.

Modelling of the (001) and (002) surfaces of LaNi₅ and the study of their interactions with H₂ molecules was performed within the slab approach using the all-electrons DFT-based FHI-aims software [56]. The slabs contained five atomic layers with the vacuum region set to about 16 \AA . The geometry of both pristine and with adsorbed H₂ surfaces was first relaxed in two steps employing first predefined “light” and then “tight” basis sets; for H only, the tight one was always selected. The PBE exchange-correlation functional [42], scalar-relativistic effect for all electrons (ZORA approximation) and a Gaussian smearing of 0.1 eV were used [57]. The Brillouin zone was sampled with a (12, 12, 2) k -point mesh. The relaxed structures were the input to undertake ED/QTAIM and ELI-D calculations with the FPLO and DGrid packages, using the same set up above-described for the bulk. Surfaces were both simulated with a H₂ coverage (defined as the number of adsorbed H₂ molecules over the number of the atoms of the first layer) of 1 monolayer (ML). Scalar fields and the related basins for both bulk and surfaces results were visualized with the aid of the Paraview application [58,59].

2.4. Catalytic test

Catalytic experiments were performed in a tubular fixed-bed silica glass reactor, loaded with 88 mg of intermetallic catalyst and 700 mg silica glass. 80 NmL/min of gaseous reactant mixture, in diluted conditions with nitrogen, were fed to the reactor with a GHSV of 55000 h^{-1} and an H₂/CO₂ ratio of 5. Three catalytic tests were conducted on the same catalyst as shown in Fig. 1, named Full Experimental Run (FER): the catalyst was tested as cast (FER0), after pre-reduction in situ under hydrogen (20% vol/vol) flow at 723 K for 1 h (FER1) and at 873 K for 2 h (FER2).

For each experiment, the reaction temperature was varied step by step from 523 to 773 K (ascending temperature) and from 773 to 523 K (descending temperature). An additional catalytic test, labeled as Short Experimental Run (SER), was performed with LN and CN intermetallic catalysts pre-reduced at 873 K for 4 h to possibly shed light on the mechanism of the catalyst activation.

The product stream composition was analyzed online by a Nicolet 6700 FT-IR instrument by means of absorbance collected at 2293, 2170, and 1333 cm^{-1} for CO₂, CO, and CH₄, respectively. The collected absorbance of each component was correlated to its concentration by a calibration curve, previously obtained by using gas mixtures with known concentrations. The flow rate of the product was measured at each temperature step to evaluate CO₂ conversion (X_{CO_2}), product yields

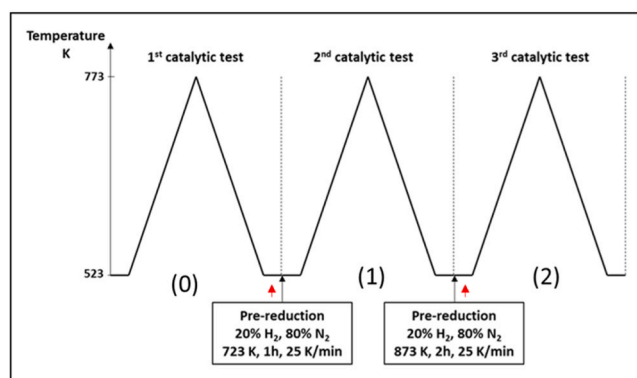


Fig. 1. Diagram of the catalytic FER test.

(Y_{CH_4} and Y_{CO}), and selectivity (S_{CH_4} and S_{CO}). These have been evaluated as shown in the Eqs. 1,2, and Eq. 3.

$$X_{CO_2} = \frac{F_{CO_2in} - F_{CO_2out}}{F_{CO_2in}} \quad (1)$$

$$Y_{CH_4,CO} = \frac{F_{CH_4,CO}}{F_{CO_2in}} \quad (2)$$

$$S_{CH_4,CO} = \frac{F_{CH_4,CO}}{F_{CO_2in} - F_{CO_2out}} \quad (3)$$

Performances of intermetallic-based catalysts have been compared to the ones achieved in the same tested conditions onto a commercial catalyst developed for CO₂ methanation and provided by Clariant (notation CL-CAT).

3. Results and Discussion

3.1. Characterization of fresh intermetallic catalysts

SEM-EDX and XRD analyses of AC, AF, and AN samples revealed that all these contain two phases: aluminum together with Al₉Co₂, Al₁₃Fe₄, and Al₃Ni, respectively. Micrographic analyses display that all the synthesized compounds have a relative phase amount in excellent agreement with the related phase diagram, with the intermetallic being the majority phase ($\geq 80\%$). Moreover, compositional EDX analyses are in line with the chosen intermetallic stoichiometry. Selected micrographs are reported in Fig. S1 (in Electronic Supplementary Information) and the measured EDX compositions are introduced in Table 1.

Indexed X-ray powder patterns are shown in Fig. S2, together with the calculated lattice parameters for each intermetallic, displaying excellent agreement with the literature data [60].

LN and CN are LaNi₅ and CeNi₅ phase pure, as shown by both SEM-EDX and XRD analyses (Figs. 2 and 3a,b). RENi₅ intermetallic ($RE = La, Ce$) crystallizes with the hexagonal *hP6*-CaCu₅ structure (Space Group: *P6/mmm*, N° 191). Obtained unit cell parameters are $a = 5.0071(1)$, $c = 3.9876(1)$ Å for LaNi₅; $a = 4.8802(1)$, $c = 4.0000(1)$ Å for CeNi₅, in agreement with literature data [60].

3.2. Chemical bonding

The RENi₅ intermetallic compounds ($RE = La, Ce$) belong to the family of the Haucke phases [61], crystallizing with the hexagonal *hP6*-CaCu₅ structure (space group: *P6/mmm*, N° 191). The RE , Ni1, and Ni2 species occupy the non-refinable 1a, 2c, and 3 g Wyckoff positions, respectively. The crystal structure may be described as a stacking of two kinds of planes perpendicular to the c axis i.e., to the [001] direction. The (001) planes are formed by a combination of a triangular layer of RE , labeled as A, and a hexagonal one of Ni1, labeled as a, (see Fig. S3), indicated then as [Aa]; the (002) planes are of a Kagomé type and are only composed by Ni2, labeled as α (Fig. S3). Therefore, the crystal structure is described by the [Aa] α stacking sequence, leading to Coordination Numbers (CN) of 18 for RE and 12 for both Ni1 and Ni2.

Table 1

Measured composition of the intermetallic phase (expressed in both at% and wt %) in the Al- M ($M = Fe, Co, Ni$) and RE -Ni ($RE = La, Ce$) samples.

IMC	Measured composition					
	Al		M		RE	
	at%	wt%	at%	wt%	at%	wt%
Al ₁₃ Fe ₄	75.0(3)	59.0(4)	25.0(3)	41.0(4)	–	–
Al ₉ Co ₂	81.5(3)	67.0(2)	18.5(3)	33.0(2)	–	–
Al ₃ Ni	74.5(1)	57.4(1)	25.5(1)	42.6(1)	–	–
LaNi ₅	–	–	82.8(1)	67.1(2)	17.2(1)	32.9(2)
CeNi ₅	–	–	82.4(2)	66.1(2)	17.6(1)	33.9(2)

Interatomic distances are listed in Table S2.

Aiming at a better understanding of the chemical behaviour of the investigated materials under reaction conditions, their electronic structure and chemical bonding were calculated and analysed. Although LaNi₅ and CeNi₅ were experimentally found to be exchange-enhanced Pauli paramagnets, first principle DFT calculations lead to spin-polarised ground states [28,62–67]. Such findings were ascribed to the relatively high density of states at the Fermi level or to the fact that the systems are close to a quantum critical point [68,69]. Thus, both non- and spin-polarised DFT calculations were performed for LaNi₅ and CeNi₅, including also a DFT+ U calculation for the latter. Magnetic moments per formula unit of 1.41 μ_B (LaNi₅), 0.83 μ_B (CeNi₅), and 0.86 μ_B (CeNi₅ - + U) were obtained, confirming the convergence to spin-polarised ground states when DFT calculations are performed. Nevertheless, no relevant differences occur among chemical bonding results obtained from the aforementioned DFT calculations. Thus, data derived from the non-spin polarised cases are presented in the following. QTAIM atomic charges, ELI-D valence basins populations and bond fractions for each performed DFT calculation are listed in Table S3 and S4.

According to the Quantum Theory of Atoms in Molecules (QTAIM) both RE bear positive effective charges. Lanthanum transfers more electrons (1.40) than cerium (1.16) toward the surrounding nickel species (Figs. S4a and 4a).

Thus, both Ni1 and Ni2 species are QTAIM anions, with effective charges comprised between -0.19 to -0.31 (Fig. 4a and S4a, Table S3).

It is worth noting that Ni2 is slightly more negative than Ni1; such difference may be initially ascribed to the different coordination environments of the two inequivalent Ni. In fact, although they both have a Coordination Number (CN) of 12, Ni1 is surrounded by 3 RE whereas Ni2 by 4 RE . The cationic behaviour of RE is also in line with the shape of the RE QTAIM basins (green basins in Fig. 4a and S4a) which is rather close to spherical. The same does not hold for Ni basins (red and orangish in Fig. 4a and S4a) showing flat surfaces with each other hinting toward covalent interactions. Similar QTAIM charges were recently reported by Mizoguchi et al. for the isostructural LaCo₅ (La: +1.28; Co1: -0.21 ; Co2: -0.28), pointing out the crucial role of negatively charged late transition metals in intermetallic hydrogenation [70]. Such anionic behavior was also described for other metallic components (e.g. Ru, Pd, Pt, Ag, Au) of intermetallic compounds [71–75] and, in some cases, related to unexpected physical and chemical properties [76–79]. An in-depth position-space bonding analysis is enabled by the Electron Localizability Indicator (ELI) and the intersection of its valence basins with the surrounding QTAIM atomic ones.

LaNi₅ and CeNi₅ exhibit a similar ELI-D spatial distribution comprising three kinds of attractors in analogous sites (see Figs. S4b-c and 4b-c). These maxima, labeled as $b1$, $b2$, and $b3$, are in the 4 h , 12o, and 12 n Wyckoff sites, respectively. This finding corroborates the idea that both the ELI-D and the ELF (Electron Localization Function) indicators may reveal crystal space regions suitable for the localization of hydrides [22,80–82]. Indeed, experimental structural data for LaNi₅ deuterides showed that such sites are generally partially occupied by the absorbed deuterium [28,83]. Each of the valence basins associated with the attractors (see Fig. 4d and S4d) is intersected by four QTAIM atoms, resulting in four-atomic (4a) bonds (see Table 2).

The multi-atomic character of such bonding basins accompanied by their low average electronic populations $\bar{N}(B_i)$ can be ascribed to the low number of valence electrons per atom [84,85]. For each basin, the Ni QTAIM atoms are those that contribute the most to the valence population. The $b1$ -basin (grey in Fig. 4d) is the only one intersected just by Ni atoms i.e., one Ni1 and three Ni2. Interestingly, the bonding pattern of elemental face centred cubic Ni is only composed by ELI-D basins located in tetrahedral holes, resulting in 4-atomic (4a) valence basins like those found within the tile compounds (see Fig. S5). Since RENi₅ are the Ni-richest phases in the RE -Ni systems, a chemical scenario

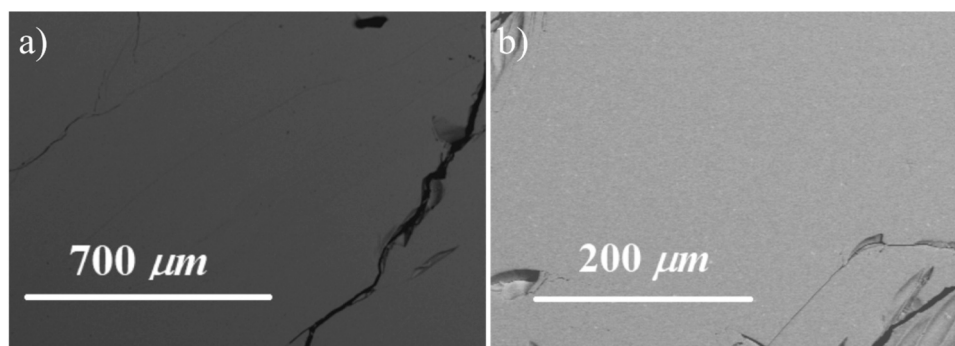


Fig. 2. SEM/BSE micrographs acquired on the LN (a) and CN (b) samples.

analogous to that in elemental nickel is retained within the 4 *h* sites. Nevertheless, some differences may be highlighted: the electronic population of the 4*a*-basins is lower for the intermetallic than in the pure element (0.62 vs 1.11); in the 1:5 stoichiometry phases the four Ni atoms involved are not symmetrically equivalent and then they do not equally contribute to the basin population. In fact, the bond fraction per atom of Ni1, $p(B_i^{Ni1})$, is slightly larger than that of Ni2, $p(B_i^{Ni2})$. The latter can be obtained from the cumulative values listed in Table 2. Considering CeNi₅, $p(B_i^{Ni2})$ is one-third of 0.72 i.e., 0.24, since three Ni2 QTAIM atoms intersect the b1 ELI-D basin. The b2 and b3 basins, represented with green and purple colors in Fig. 4d, are both intersected by 3Ni and 1RE, with the latter being the minor contributor, leading to low bond fractions $p(B_i^{RE})$ ranging in-between 0.05–0.07 (Table 2). Hence, such basins should be interpreted as polar 4-atomic interactions.

The main difference in the ELI-D topology among LaNi₅ and CeNi₅ occurs in the (001) planes, where RE–Ni1 bonds are indicated by ELI-D attractors only in the case of RE = Ce. Nevertheless, a careful analysis of the ELI-D basins reveals that differences in topology do not correlate with a pronounced difference in chemical bonding. Focusing on LaNi₅, the presence of La–Ni covalent bond is revealed by the shape of the penultimate shell basin of Ni1 (Fig. 5, left).

It has three bulges (dashed circle in Fig. 5, left) that extend in the valence region toward the surrounding La. Moreover, each bulge is intersected by one La QTAIM atom giving rise to quite unusual scenario for penultimate shell basins that are generally completely inside the corresponding QTAIM basin. A very similar scenario was recently reported for La/Yb/Eu–Pd, La–Ag, and La–Au bonds in La₂PdGe₆ [71,86], Yb₂PdGe₃ [87], and EuPdSn₂ [88], La₂AgGe₆ [71] and LaAuMg₂ [73] all indicated by bulges of the transition metal (*T*) penultimate shell basins and interpreted as two-atomic (2*a*) polar covalent metal-metal interactions. It was also found that by changing the RE metal from La to Y in RE₂PdGe₆, the Y–Pd bond was indicated by ELI-D attractors and then by the corresponding basins, resulting in the absence of bulges on the Pd penultimate shell. Likewise, when changing from La to Ce, the Ce–Ni bond is clearly indicated by bonding basins (Fig. 5, right) which are exclusively intersected by these two atoms, leading to bond fractions $p(B_i^{Ni1}) = 0.87$ and $p(B_i^{Ce}) = 0.13$, which support the polar nature of this 2*a* interactions. It is worth mentioning that RE–Ni1 distances ($d_{La-Ni1} = 2.89$ Å; $d_{Ce-Ni1} = 2.82$ Å) are much shorter than the RE–Ni2 ($d_{La-Ni2} = 3.20$ Å; $d_{Ce-Ni2} = 3.16$ Å), well in line with these outcomes. Such results constitute a further extension in the study of RE–*T* interactions. In conclusion, each La and Ce establishes six of such 2*a* bonds (see Fig. 5), and each Ni1 is then bonded to three La/Ce species, forming infinite planar two-dimensional layers $\infty [RENi_2]$. The overall bonding scenario may be described as an interplay of three types of four-atomic (4*a*) interactions, realized in the crystal space between the [Aa] and the α layers, and of two-atomic 2*a* polar covalent RE–Ni1 bonds within the [Aa] planes. These results constitute one more example of the chemical differences between intermetallic phases and elemental metals or substitutional alloys, making them potentially attractive as new

heterogeneous catalysts. Additionally, the obtained bonding results constitute the basis to understand the chemical behavior of the studied intermetallics and are suited to drive the investigation of the processes taking place at the IMC surfaces, e.g. absorption and dissociation of H₂ molecules.

3.3. Characterization of pre-reduced intermetallic catalysts

With the aim to evaluate the mechanism of the catalyst activation, LN and CN intermetallic catalysts were pre-reduced at 873 K for 4 h and then characterized, establishing the state of catalytic material prior to the SER tests.

In Fig. 3 c and d, X-ray diffraction patterns of reduced LN and CN evidenced that both LaNi₅ and CeNi₅ partially decompose to metallic Ni and the corresponding oxides i.e., La₂O₃ and CeO₂, respectively. After an accurate profile fitting, the relative phases amount was evaluated in weight %, and calculated for LN as 79% of LaNi₅, 17% Ni and 4% La₂O₃; whereas for CN, 81% of CeNi₅, 14% Ni, and 5% CeO₂. These results point toward a similar decomposition behavior of the studied intermetallics under the applied conditions and are in good agreement with literature data reported for the hydrogenation process [89]. Nevertheless, the mechanism that leads to the oxide formation is still not completely clear.

In addition to the structure analysis, the morphology of the sample was investigated by means of FE-SEM. Focusing on LN, the observed surface roughness, extended to the whole sample, may be an indication of the LaNi₅ decomposition (Fig. 6a, b). As clearly visible in Fig. 6a, such decomposition is more pronounced close to defects and cracks where probably the process originated. Moreover, in Fig. 6b rounded particles of variable dimensions, ranging from about 100–150 nm, can be envisaged; their measured EDX compositions reveal that Ni is still the most abundant component.

Additionally, also La-richest extended particles, irregularly shaped, were detected; at the surface, EDX analysis displays the presence of oxygen, well in line with the formation of La₂O₃ observed from X-ray analysis (Fig. 6b).

The CN measured EDX composition of the fresh material is in excellent agreement with the CeNi₅ stoichiometry, whereas for the reduced CN sample a composition inhomogeneity extended to the whole sample was observed hinting toward its decomposition. In fact, compared to LN, a tiny number of rounded particles can be envisaged, as shown in Fig. 6c, d.

3.4. Effect of hydrogen at the clean surface

The (001) and (002) surfaces, namely [Aa] and α , respectively, (see Fig. S3), were considered to investigate their interactions with H₂ molecules. The clean (001), often also indicated as (0001) in hexagonal systems, is usually selected in the literature for surface simulations and for adsorption studies of gases e.g., H₂O, CO, CO₂ and H₂, as it is known to have relatively low surface energy and to pulverize along such a

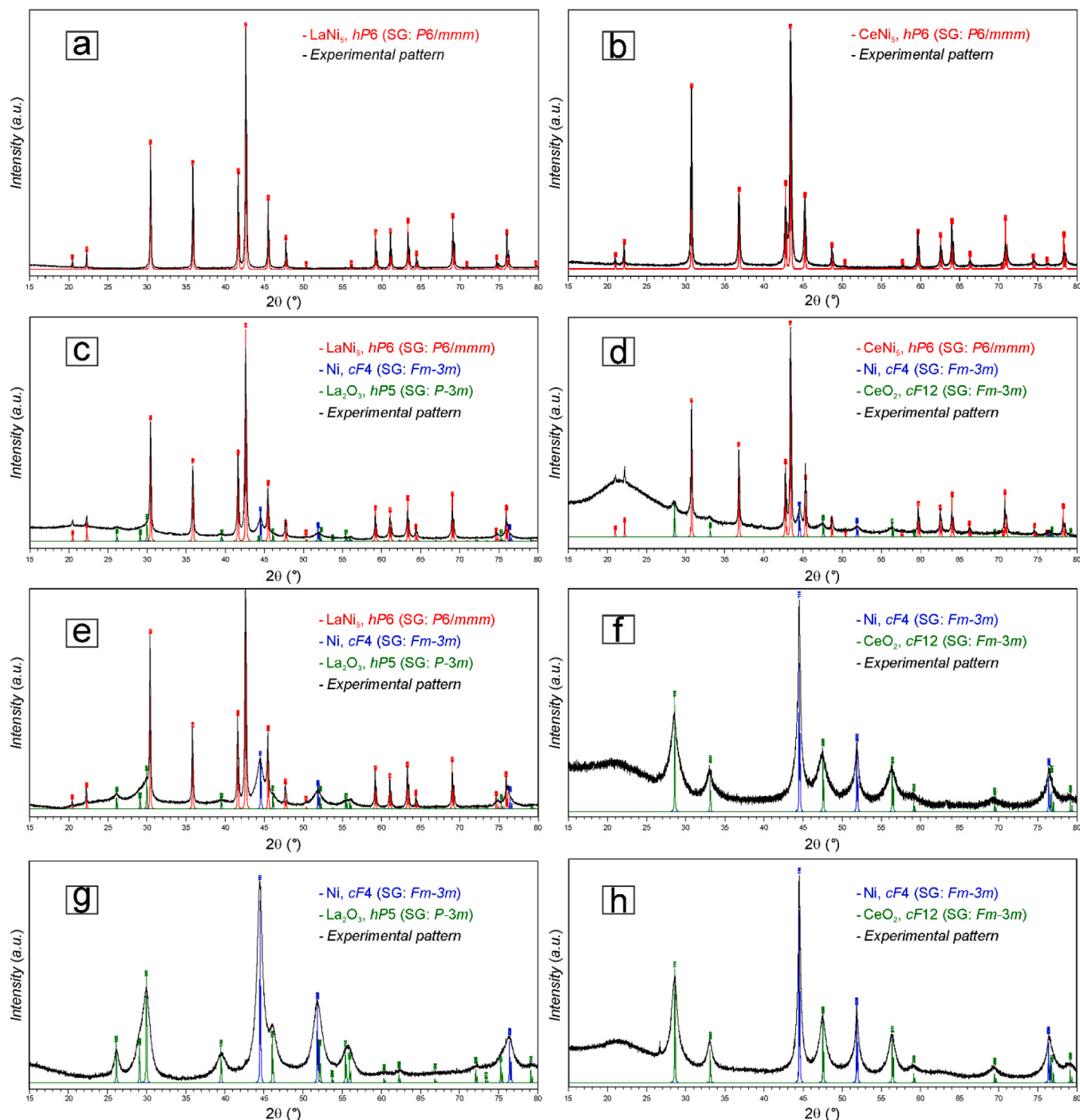


Fig. 3. Indexed X-ray powder patterns of LN and CN samples before the catalytic tests (a, b), pre-reduced (c, d), at the end of the SER (e, f) and FER (g, h) tests.

surface during adsorption/desorption cycles [90,91]. Interactions with H_2 are indeed interesting, as they were experimentally found to induce the decomposition of both LaNi_5 and CeNi_5 phases during the pre-reduction treatment (see SER experiment), thereby enhancing the catalytic activity.

To conduct this study, the bonding results described in this work based on ELI-D/QTAIM analysis for the bulk materials constitute an essential starting point. The ELI-D approach for the prediction of potential adsorption sites was recently introduced by Villaseca *et al.* [92], turning out to be an effective and computationally non-demanding tool for the characterization of the entire surface through its complete real-space mapping, by investigating CO adsorption sites on the $(\bar{1}\bar{1}\bar{1})$

GaPd surface. The presence of unshielded Pd anions and dangling bonds partially shielding the Ga cations, hinted toward the adsorption of CO molecules on top of the Pd species, via the formation of polar covalent C-Pd bonds. The same approach has been here applied to H_2 adsorption, and eventual dissociation, at the LaNi_5 surface. In comparison to the case of CO-GaPd, some differences need to be taken into consideration. In fact, once an ELI-D surface mapping is obtained, the selection of the appropriate adsorption site also depends on the type of adsorbate under consideration. In the case of CO, the presence of a lone pair on the C atoms causes a strong repulsion when it approaches the dangling bonds shielding a large surface portion. Thus, suitable sites were found in correspondence of surface region with a lower electron localizability *i.*

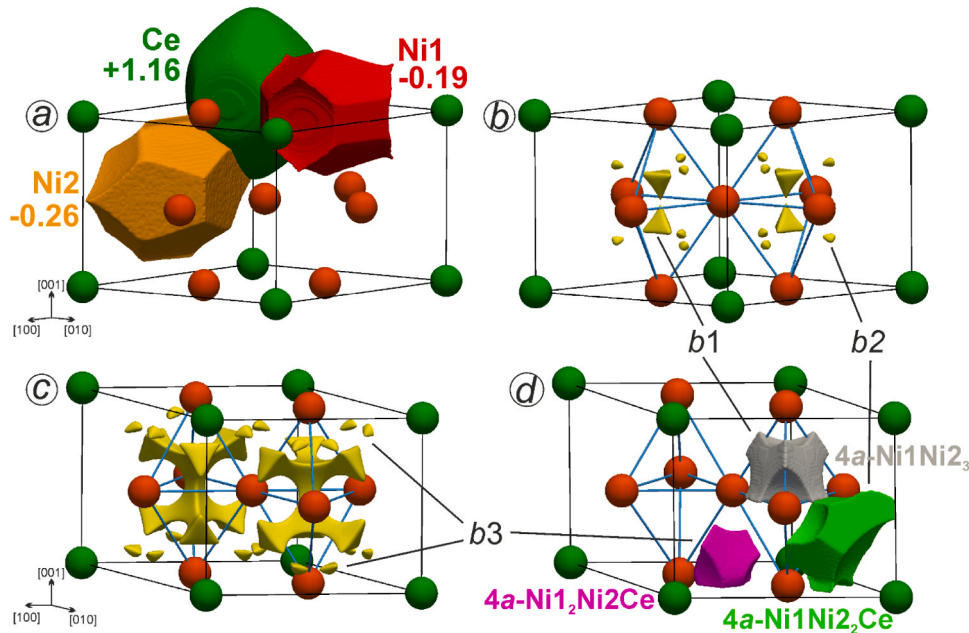


Fig. 4. Chemical bonding in CeNi_5 : (a) shapes and effective charges of the QAIM atomic basins; (b, c) 0.969- and 0.941-localization domains signifying ELI-D attractors located in the 4 h , 12 o and 12 n sites, labeled as $b1$, $b2$ and $b3$, respectively; (d) shapes and atomicity of the ELI-D valence basins. As a guide to the eye, the Ni–Ni contacts are indicated by light-blue sticks.

Table 2
Atomicity, average electronic population, and bond fraction for each ELI-D valence basin of LaNi_5 and CeNi_5 .

Compound	ELI-D basin (B_i)	Atomicity $\text{Ni}_1\text{Ni}_2\text{Ni}_3\text{RE}$	$\bar{N}(B_i)$	$\sum_{j=1}^k p(B_i^{\text{Ni}_j})$	$\sum_{j=1}^x p(B_i^{\text{Ni}_j})$	$p(B_i^{\text{RE}})$
LaNi_5	$b1$	$\text{Ni}_1\text{Ni}_2\text{Ni}_3$	0.623	0.303	0.697	–
	$b2$	$\text{Ni}_1\text{Ni}_2\text{Ni}_3\text{La}$	0.607	0.285	0.653	0.062
	$b3$	$\text{Ni}_1\text{Ni}_2\text{Ni}_3\text{La}$	0.250	0.613	0.332	0.055
CeNi_5	$b1$	$\text{Ni}_1\text{Ni}_2\text{Ni}_3$	0.626	0.276	0.724	–
	$b2$	$\text{Ni}_1\text{Ni}_2\text{Ni}_3\text{Ce}$	0.611	0.292	0.637	0.071
	$b3$	$\text{Ni}_1\text{Ni}_2\text{Ni}_3\text{Ce}$	0.264	0.605	0.333	0.062
	Ce–Ni	Ni_1Ce	0.040	0.867	–	0.133

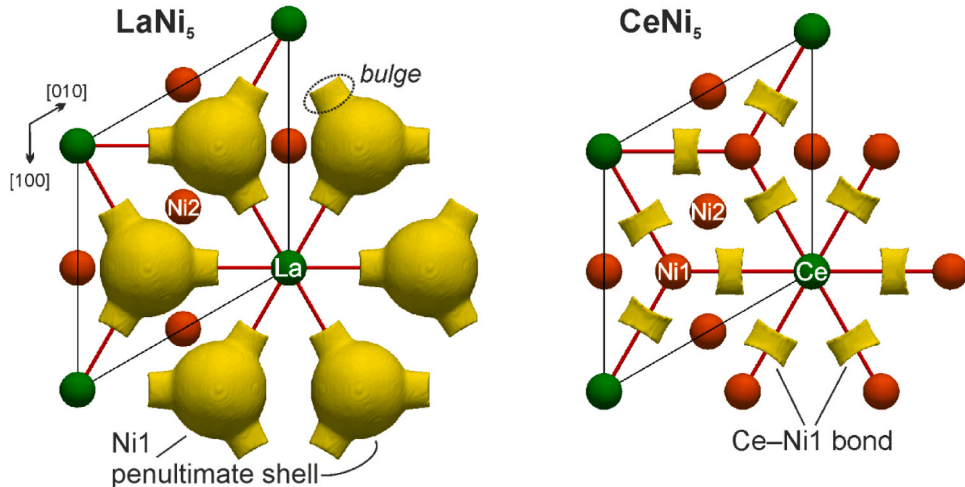


Fig. 5. RE–Ni interactions in the (001) planes indicated by bulges of the Ni1 ELI-D penultimate shell basins for LaNi_5 (left), and by 2-atomic Ce–Ni1 bonding basins for CeNi_5 (right).

e., in correspondence with Pd atoms. For the H_2 – LaNi_5 system, an opposite scenario may be expected. As already evidenced in several studies, hydrogen atoms within pure metals and IMCs tend to occupy regions with high values of ELF and/or ELI-D [80–82]. Furthermore, it

has been recently shown that high ELF values at the surface allow the prediction of hydrogen absorption sites on the surface of metallic Mg [93]. Consequently, in the present study, it is assumed that surface regions corresponding to dangling bonds may act as suitable sites for H_2

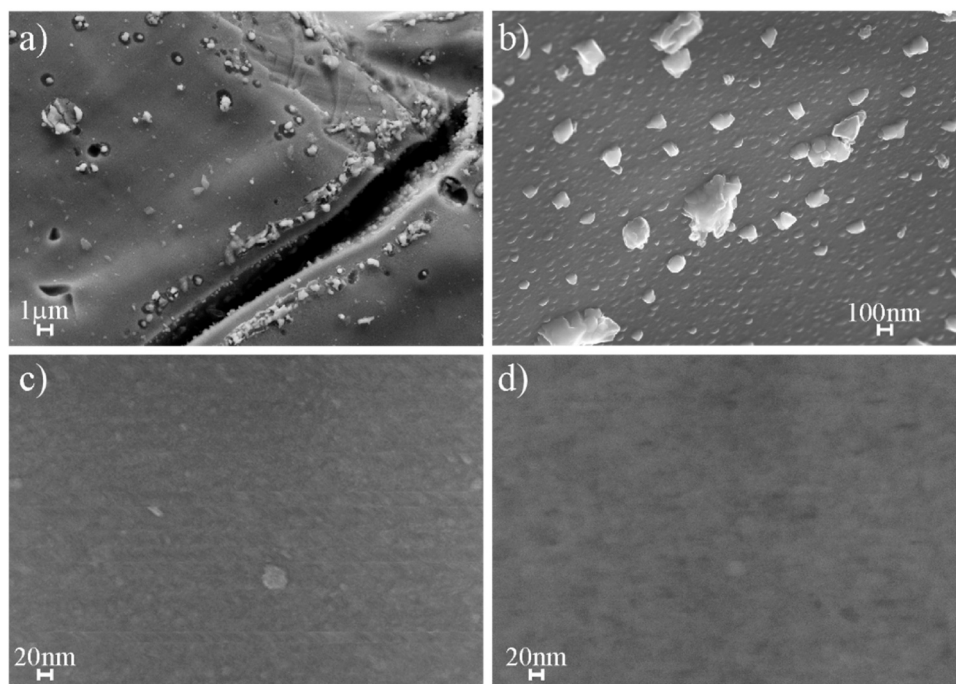


Fig. 6. FE-SEM micrographs of the reduced LN and CN samples. LN images acquired in SE mode at lower (a) and higher (b) magnification; CN image of the same region acquired at 400.000X with both SE (c) and BSE (d) signals.

molecules. Thus, the ED and ELI-D were both calculated and analysed for the α and [Aa] surfaces of LaNi_5 . After structural relaxation they both retain the same atomic arrangement shown in the bulk, thus indicating their good stability. The [Aa] surface is composed of both La and Ni1 in a 1:2 ratio, while the α one is only constituted by Ni2 species. QTAIM effective charges on the surface La (+1.3) and Ni1 (−0.6) additionally support the stability of the [Aa] layer which is almost neutral; to accomplish it, Ni1 charge at the surface is larger than in the bulk (−0.6 vs

−0.2). Moreover, the La–Ni1 2-center bonds parallel to the cleavage direction are preserved. The same is not true for the α surface with Ni2 effective charges of −0.2, which are also analogous in the subsurface layer and in the bulk. In both cases, subsurface QTAIM charges are comparable with those of the bulk structure. The ELI-D distributions represented in Fig. 7 show that dangling bonds occur both on the α (top) and [Aa] (bottom) surfaces. They originate from the $b1$ (α) and $b3$ (Aa) ELI-D attractors due to the missing of an upper Ni1 and Ni2 atom,

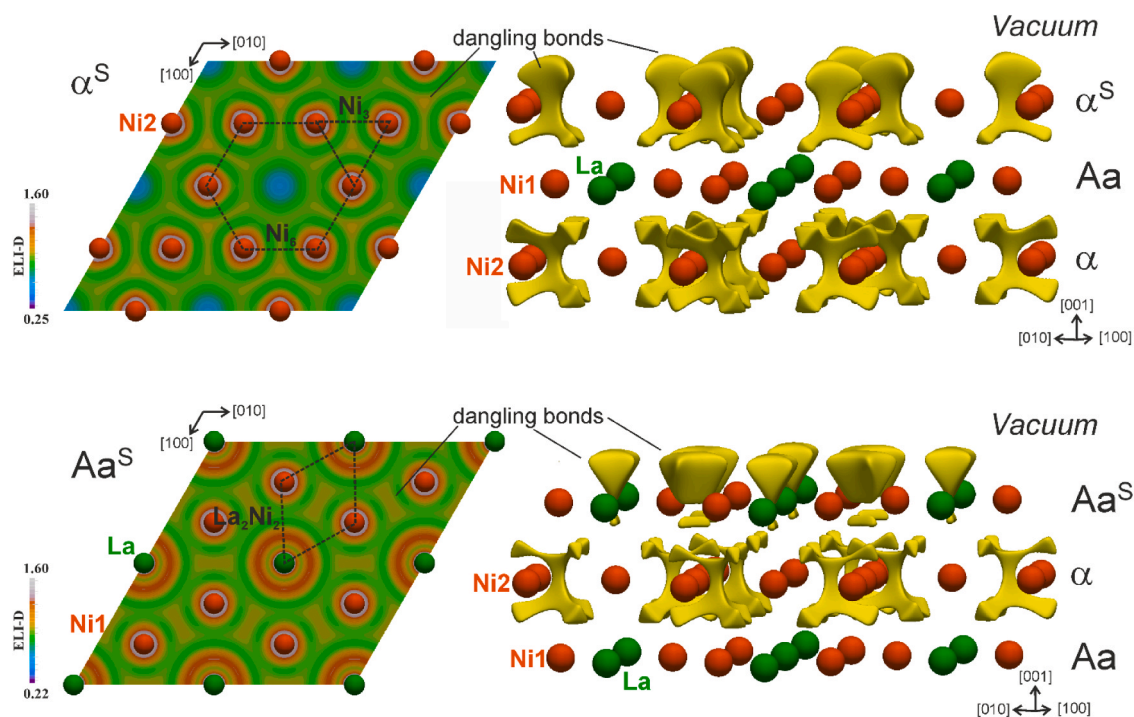


Fig. 7. ELI-D planar distribution (left) and isosurfaces (right) in the α (top) and [Aa] (bottom) pristine surfaces of LaNi_5 . The dashed polygons delimit the Ni_6 , Ni_3 and La_2Ni_2 sites where the H_2 molecules have been adsorbed. The superscript “S” serves as a guide to eye to discriminates the surface planes from the subsurface ones.

respectively, resulting in $3a$ -basins that extend in the vacuum. ELI-D isosurfaces displayed for the subsurface crystal space (Fig. 7, right) reveal a topology almost identical to the bulk (see Figs. S4c and 4c). As anticipated, sites with a high electron localizability may be effectively considered good adsorption sites for H_2 molecules. At the same time, it is worth noting that although both α and [Aa] surfaces have cavities of suitable dimensions to accommodate H_2 , they do not always coincide with dangling bonds. In fact, such bonds are in Ni_3 (Fig. 7, top left side) and La_2Ni_2 (Fig. 7, bottom left side) holes, although the largest one is the Ni_6 one (Fig. 7, top left side) which corresponds to a region of low ELI-D values.

To validate the here proposed approach, the H_2 molecules were adsorbed not just in the Ni_3 and La_2Ni_2 holes, but also in correspondence of the largest Ni_6 (Fig. 8, top). The possibility to perform such a simulation and approach validation in correspondence of the Ni_6 site is a relevant factor making the α surface of great interest for the actual study. In the case of the [Aa] surface, H_2 molecules were adsorbed both perpendicularly and parallelly to the surface. The latter configuration was tested as well since the dangling bonds at the [Aa] surface originate from two b3 type of coplanar ELI-D attractors (Figs. S4c and Fig. 4c) that are only 0.32 Å apart from each other.

The slab structures resulting after adsorbing H_2 molecules on top of the selected surfaces based on dangling bond distributions, were then relaxed allowing the atomic positions to vary, aiming at minimizing the total energy of the system. It is then important to keep in mind that it does not represent a temporal evolution of the system. The resulting $LaNi_5$ -H slab structures are displayed in Fig. 8, bottom. Two main results are detected: 1) H_2 molecules adsorbed in correspondence of dangling bonds dissociate, with the contemporary penetration of H atoms into the subsurface space; 2) the H_2 dissociation is accompanied by hydrogen atoms reduction to hydrides and the contemporary oxidation of Ni anionic species. Focusing on the first result, it is worth pointing out that H_2 molecules dissociate if and only if they are adsorbed in correspondence with dangling bonds (see red H atoms in Fig. 8). In fact, H_2 molecules adsorbed on the largest Ni_6 cavities are not dissociated at the end of the relaxation procedure (H-H distance after relaxation is 0.751 Å) but are even pushed upward at about 3.2 Å above the α surface (see blue H atoms in Fig. 8, left). This outcome validates the proposed approach and highlights that the formation of an interstitial

intermetallic hydride is not simply due to dimensional i.e., hole size, but also to chemical factors. The distribution of Ni_2 atoms in the relaxed α surface (Fig. 8, left bottom) is not affected by the hydride formation, preserving the Kagomé planar structure. QTAIM effective charges of each H (red in Fig. 8, left bottom) are -0.3 , whereas the H species bonded in H_2 molecules (blue in Fig. 8, left bottom) hold a 0.0 charge, as expected; Ni_2 atoms at the surface reduce their charges to $+0.2$ whereas those in the subsurface region retain the -0.2 charge. Focusing on the [Aa] surface, the relaxed slab structures differ depending on the initial orientation of H_2 with respect to (001) i.e., perpendicular, or parallel. In the first case (Fig. 8, middle bottom), Ni_1 species move upward by 0.56 Å, becoming neutral (QTAIM charge: 0.0) whereas La slightly increases its charge to $+1.6$. This effect is greater in the second case (Fig. 8, right bottom) leading to a surface reconstruction. In fact, Ni_1 species move upward by 1.76 Å with respect to the La atoms, giving rise to a new surface only composed of Ni_1 ($+0.2$) and H, with the first subsurface layer being only formed by La ($+1.6$). It is interesting to note that H species in both cases always hold the same -0.3 charge, as in the relaxed H- $LaNi_5$ α case. Finally, it is worth noting that the slab model displaying a reconstructed surface (Fig. 8, right bottom) is more stable than the other one (Fig. 8, middle bottom) by -2.86 meV/at. Such findings, in addition to the Ni reduction, detected in all three studied scenarios, with charges ranging from 0.0 to $+0.2$, are well in line with the formation of metallic Ni, experimentally detected. It may be then concluded that the interaction of H_2 with the pristine IMC surfaces is one of the factors inducing its decomposition.

3.5. Assessment of catalytic performances

Catalytic performances have been evaluated according to the scheme reported in Fig. 1 (Full Experimental Run - FER). For most active materials i.e., $RENi_5$, also a prereduction at 873 K for 4 h has been carried out on the as-cast sample prior to the catalytic experiment (Short Experimental Run SER).

Among Al-containing materials only AN had a measurable catalytic activity in chosen conditions while AF and AC were inactive for the whole test (FER); the relative absorbance profiles are reported in Fig. S6 for CO (A) and methane (B) in increasing and decreasing temperature experiments. Catalytic activity results of the AN sample are reported in

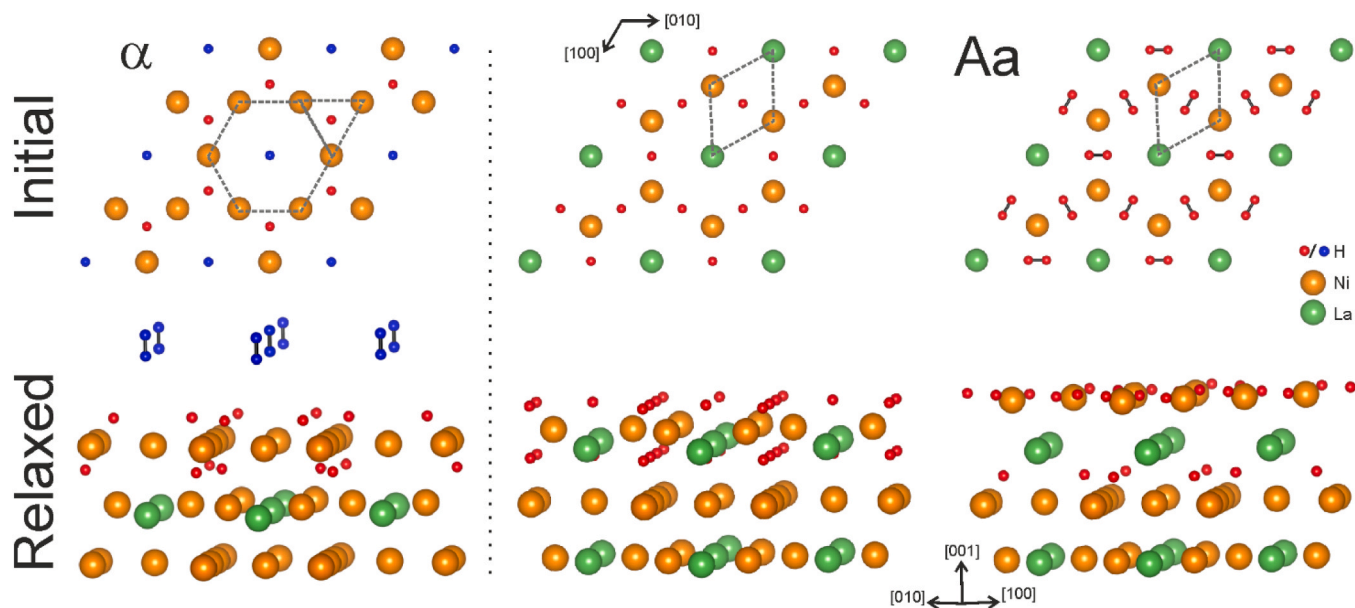


Fig. 8. α (left) and [Aa] (middle, right) surfaces of the H- $LaNi_5$ systems. In the upper part, H_2 molecules are adsorbed perpendicularly (left, middle) and parallelly (right) to the α and [Aa] surfaces on top of the sites delimited by the dashed polygons. The red H_2 molecules are located corresponding to dangling bonds, unlike the blue ones. In the lower part, the surfaces resulting from structural relaxation are shown.

Fig. S7. As cast AN sample (FER0) resulted in a completely inactive material in the whole reaction range in CO₂ hydrogenation in both Sabatier's and reverse Water Gas Shift (rWGS) reactions. After pre-reduction at both 723 (FER1) and 873 K (FER2), methane is not observed among products where only CO has been detected. AN_723K (FER1) showed a slight activity in CO production above 673 K with a yield of 5% max., which is completely lost in the decreasing temperature experiment. Reduction at 873 K is even reducing the catalytic activity of AN to zero (FER2). Interestingly, for AN_723K it is observable a decrease in CO production at constant temperature, suggesting the occurrence of partial deactivation toward rWGS (FER1).

Catalytic performances have been slightly improved in the case of LaNi₅ catalysts, even though the as-cast sample is still inactive (FER0); upon reduction at 723 K (FER1) a quite remarkable CO production is observed with an activation step at 773 K reaching a yield of 5%. In the decreasing temperature experiments, obtained yields are slightly higher than those obtained in the increasing one and, below 673 K the sample is mostly inactive. An increase in the reduction temperature (FER2) produces a more active catalyst; in this case, CO₂ conversion started at 623 K with CO as the main product. A remarkable activation step has been observed at 773 K with enhanced performances in the decreasing temperature experiment, as can be seen in Fig. 9.

The only intermetallic compound, showing remarkable activity when used as cast, is CeNi₅, with the production of both CO and CH₄ starting from 723 K in ascending temperature, but then with a higher performance in the decreasing one, being inactive only at the lowest temperature 523 K, as observable in Fig. 10.

By looking at increasing temperature performances, the highest yield to methane (25%) is reached at 723 K with an important coproduction of CO (15%), while in the decreasing temperature experiment, the catalyst resulted more active and more selective to methane with a maximum yield of 27% within the measured activity in the range 773–523 K. Moreover, by looking at the absorbances profiles it is possible to identify a marked activation occurring in transient condition in-between 673 and 723 K with a first flexum in CO production followed by a sharp increase of both CO and CH₄ absorbances, and an observed slight deactivation toward methane in the steady state time at 723 K, confirmed by the achieved catalytic activity. Prereduction at 723 K (FER1) confirmed the achieved activation by further increasing both conversion and selectivity to methane and by reaching a proper quasi-steady state condition, with a slight but observable deactivation at 573 K; in these cases, the maximum selectivity to methane is observed at 623 K (100%, 37% yield)

while maximum activity is observed above 673 K with a different ratio in-between CO and CH₄ that increases upon temperature increase. In this case, the performances resulted quite stable over the decreasing temperature ramp, even though a slight deactivation might be observed by looking at the whole yield/temperature plot for temperature lower than 673 K. The conditions applied in FER2 in a subsequent cycle reduced catalytic performances in the whole temperature range when compared with FER1 and a more pronounced rWGS activity is observed in the range 623–773 K with yields of approx. 5–20%. Again, achieved performances are stable in the decreasing temperature experiment but it is interesting to observe that the production rate of CO is in this case mostly the same as the one achieved on the as-cast sample, despite the higher performance in Sabatier's reaction, suggesting that reaction atmosphere play a crucial role in the active phase production and stabilization.

Single prereduction at 873 K for 4 h (SER) has been carried out to evaluate the role of H₂ pre-treatment at high temperatures starting from a freshly prepared intermetallic material. In the case of LN, catalytic performances appear to be a little bit improved but still in fully differential regime (max CO yield lower than 5%) for both increasing and decreasing temperature experiments (Fig. 11 left). However, differences can be appreciated by looking at the profile over time (Fig. 11 right) where at 773 K both CO and CH₄ are detected with an increasing trend over time, occurring with the same slope and achieving high activity at 723 K in decreasing temperature.

This suggests that the pool of reactants and products are responsible to carry out activation upon time on stream. A similar situation, even though with a more marked activity is observed for CN catalysts, where the performance is increased for methane but even more markedly for CO with a maximum yield of 49% and 20% at 723 and 773 K, respectively, when compared to CN_723K (FER1). The catalyst is still active in the decreasing temperature experiment, even though a slight deactivation is observed for both methane and CO below 723 K.

Moreover, the high content of nickel in presently studied catalysts are in line with some system developed in the literature (13–70 wt%), also among commercial formulations [6]. In the present case, for a straightforward comparison, obtained results over intermetallics have been compared with those arising from a Clariant's CO₂ methanation catalyst developed for SNG production, labelled as CL-CAT. The obtained results are reported in Fig. 12 and clearly show that, except for the lowest tested temperature, data are superimposed to the forecasted thermodynamic equilibrium, with a slight deviation only at 773 K,

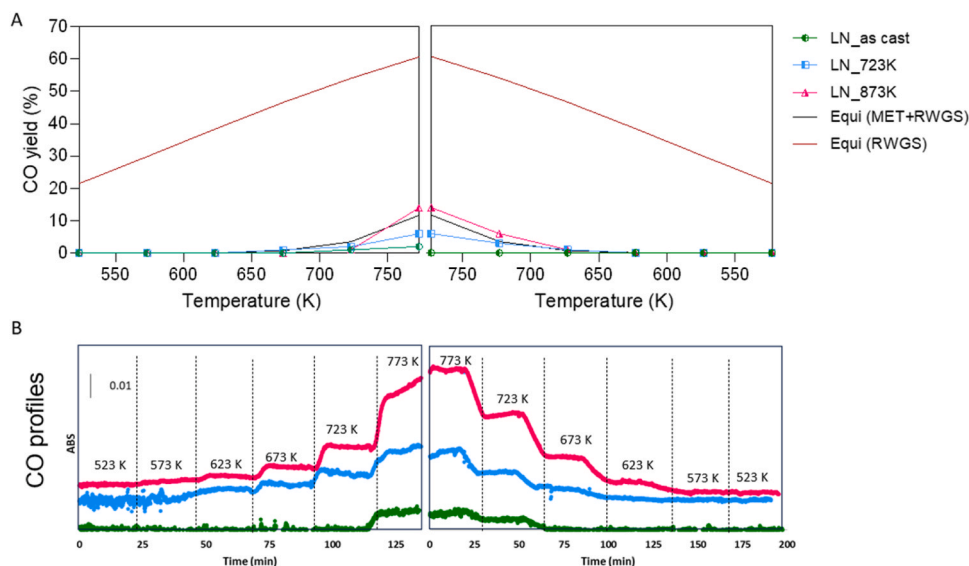


Fig. 9. CO yields and forecasted thermodynamic equilibrium (A) and CO absorbance profiles (B) of LaNi₅ in FER CO₂ methanation in the 523–573 K temperature range.

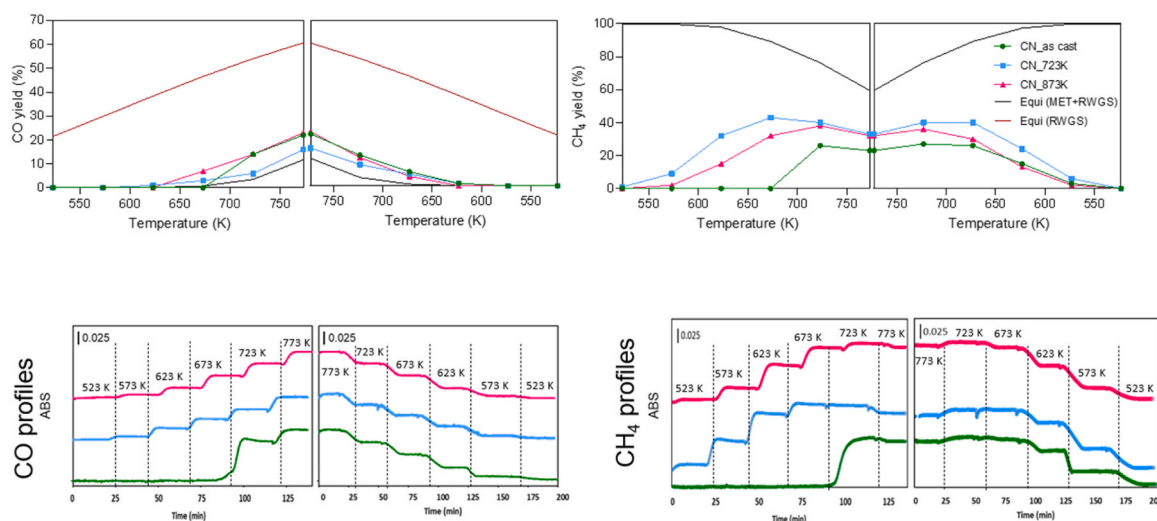


Fig. 10. Methane, CO yields and forecasted thermodynamic equilibrium (top) and methane and CO absorbance profiles (bottom) of CeNi₅ in FER CO₂ methanation in the 523–573 K temperature range.

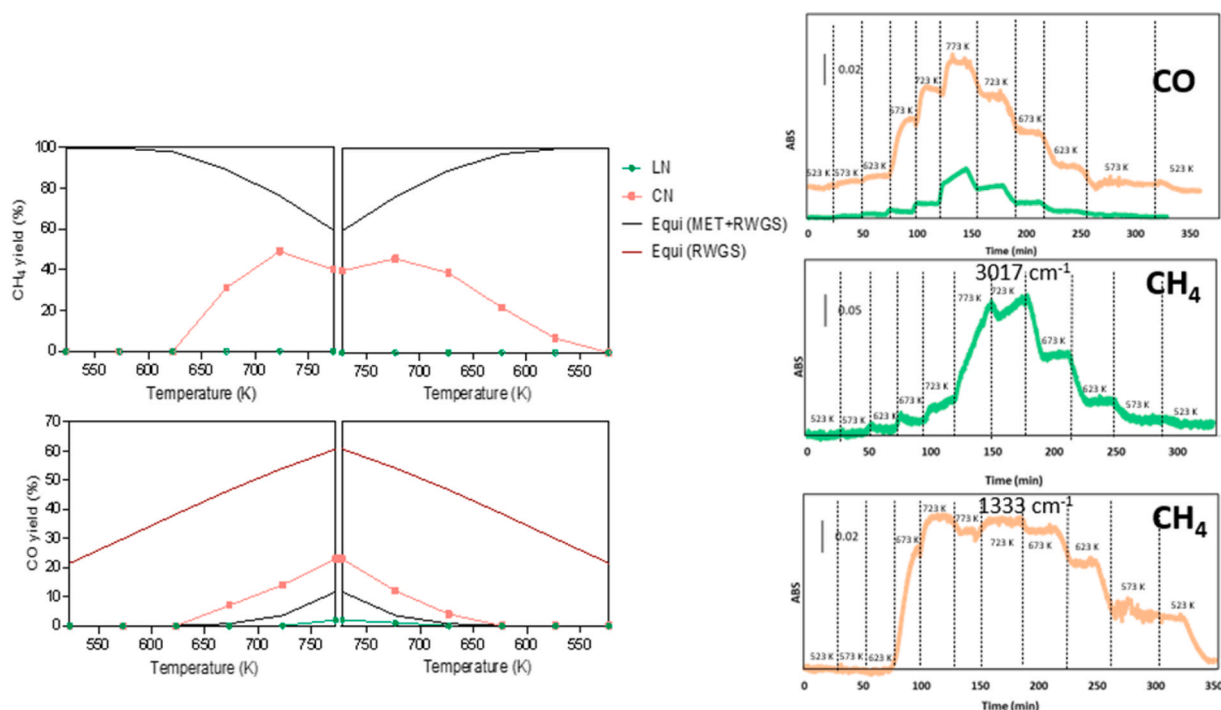


Fig. 11. Methane, CO yields and forecasted thermodynamic equilibrium (left) and methane and CO absorbance profiles (right) of LaNi₅ and CeNi₅ in SER CO₂ methanation in the 523–573 K temperature range.

similar to the one observed for Si-containing Ni/Al₂O₃ catalysts [94,95]. In this case, the maximum yield of commercial catalysts approaches 100% when tested at 573 K and 55000 h⁻¹.

3.6. Characterization of exhausted intermetallic catalysts

After catalytic tests all the materials have been characterized by X-ray powder diffraction and, LN and CN samples also by FE-SEM, to evaluate structural and morphological catalyst modifications.

AN, AF and AC powder patterns display no differences with respect to the fresh materials, as shown in Fig. S2.

Focusing on active LN and CN, the decomposition detected during the reduction treatment proceed also during the catalytic SER test,

although their behavior is different, as evidenced in Fig. 3e and f. In fact, for LN, LaNi₅ remains the majority component (56%) together with Ni (33%) and La₂O₃ (11%), while for CN the CeNi₅ intermetallic is below the detection limit so that only Ni and CeO₂ are revealed with a weight percentage of 59% and 41%, respectively. The average crystallite size of Ni and RE oxides, calculated according to the Scherrer's formula as described in paragraph 2.2.2, are 8.6 and 8.4 nm for Ni and La₂O₃, respectively, and 10.8 and 6.4 nm for Ni and CeO₂, respectively.

After FER catalytic tests, diffraction patterns show that, in addition to CeNi₅, also LaNi₅ is completely decomposed (see Fig. 3g,h). Only for CN, already completely decomposed after the SER treatment, a size increase of the Ni and CeO₂ crystallites can be observed, which almost double their diameters to 21.6 and 10.0 nm respectively, as calculated

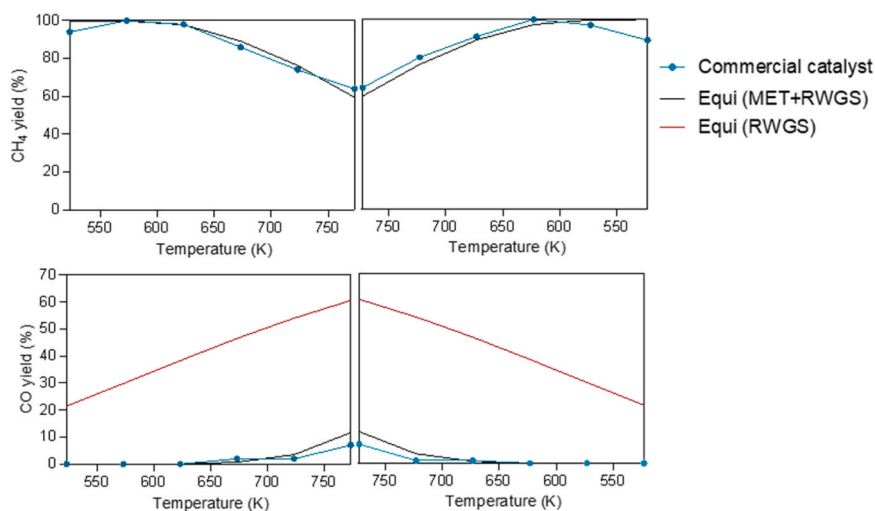


Fig. 12. Methane and CO yields of commercial catalyst in CO₂ methanation and forecasted thermodynamic equilibrium in the 523–573 K temperature range.

thanks to the Scherrer equation.

The samples morphology after catalytic tests for both materials is related to the progression of the intermetallic decomposition process, which started in the pre-reduction step. For instance, for LN, analogously to the reduced sample, after SER test, the presence of irregularly shaped La-rich crystals (see Fig. 13 a, b), rounded Ni-rich particles (see Fig. 13 a, b, c) was observed together with a matrix constituted by LaNi₅ whose decomposition is still in progress.

In fact, with respect to the annealed intermetallic, the matrix composition is Ni-poorer (62 wt% vs 67 wt%), comparable in La (31 wt% vs 33 wt%) and with the additional presence of oxygen (7 wt%).

Moreover, focusing on CN, a surface richer in cracks and defects is observed compared to the pre-reduced one, in accordance with the decomposition advance (Fig. 13d). In the same figure, the BSE compositional contrast confirms the widespread composition inhomogeneity. Nevertheless, the formation of a larger amount of spherical nano-aggregates with respect to the reduced material is observed (Fig. 13e). Moreover, the EDX composition on each sampled point and area was

never close to that of CeNi₅, in agreement with XRD results.

After FER test also the LN morphology further changes, increasing cracks and defects. The total decomposition of the intermetallic is also observed to give a matrix and crystals with different compositions. The matrix no longer has the composition of the intermetallic but is poorer in Ni (55 wt% vs 67 wt%), La-richer (37 wt% vs 33 wt%), and with oxygen (wt.8%), while the larger crystals are very rich in La (up to 70 wt%), and the smaller ones are the richest in Ni (up to 82 wt%).

Results obtained from catalytic tests, surface simulations, and characterization of freshly reduced catalytic materials are in excellent agreement.

In agreement with the above-discussed data, it is well known that upon hydrogenation, LaNi₅ is reduced into fine powder and shows surface segregation into Ni nanoparticles and La oxide [28]. The formation of Ni clusters upon cycling was also detected by in situ measurements performed by Blach and coworkers [96].

Well in line with these literature data, computational results presented in this work reveals that the interaction between LaNi₅ and pure

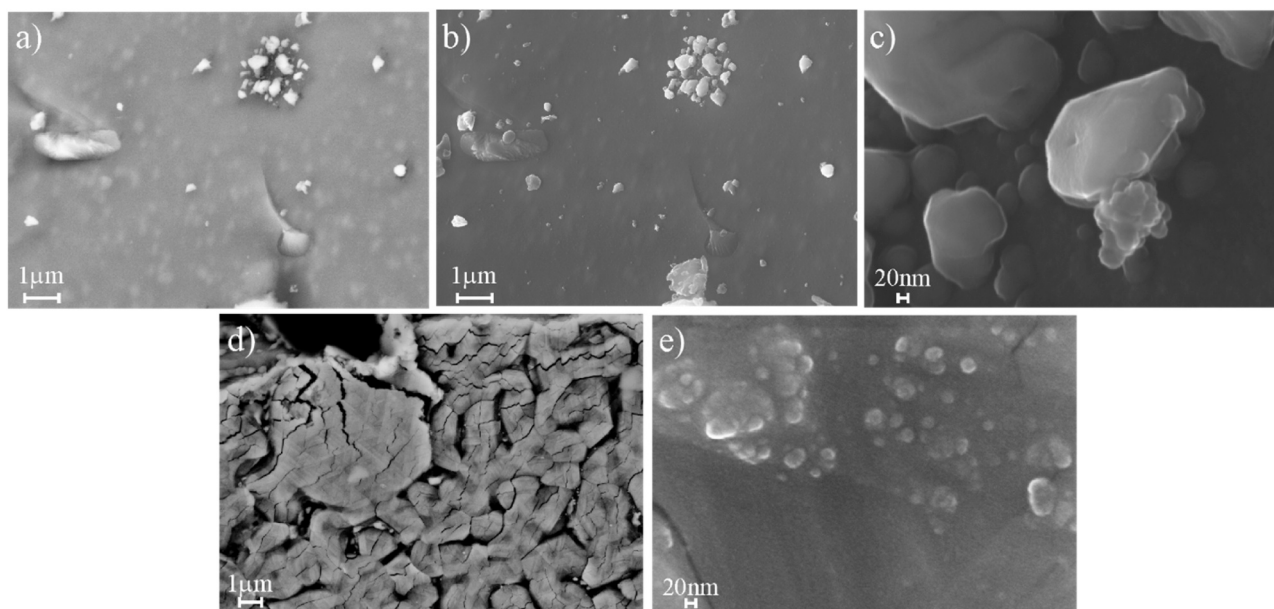


Fig. 13. FE-SEM micrographs of the exhausted (SER) LN and CN catalysts; a, b) LN images of the same region acquired with BSE and SE signals showing an elongated white La-rich crystal together with rounded Ni-rich particles; c) magnification on Ni-rich rounded particles; CN images acquired in BSE mode at lower (d) and in SE mode at higher (e) magnification.

H₂, may induce Ni(O) formation and its segregation toward the surface.

Moreover, this behaviour upon hydrogenation was related by Buschow to the small impurities always present at the surface and, possibly, on the gas [97].

The experimental conditions applied in the pre-reduction treatment are anyway different compared to those generally reported, as in our experiments high temperatures are reached; nevertheless, the presence of both Ni(O) and La₂O₃ was observed as well.

Oxidation of LaNi₅ IMCs upon catalytic experiment might arise from the interaction with water vapor, a co-product of the Sabatier reaction, that has a well-known effect on intermetallic ageing when traces of oxygen and water vapour are present; this could in principle reduce the LaNi₅ hydrogen storage capacity, [97] that in the present case is far less important. A similar situation possibly occurs for both Ce and La, but for Ce-containing IMCs only few reports are available, and it appears to be complex to retrieve catalytic data for suitable comparison of the performances.

According to Buschow [97], the formation of Ni clusters can be induced by the partial pressure ratio p_{H_2}/p_{H_2O} and this appears as a critical step for LaNi₅ poisoning in relation to H₂ adsorption; this effect, during a catalytic test, might be even more important and, possibly, justifying the prominent catalytic activity toward CO. On the other side, data for LaNi₅, used as H₂ storage and purification material, pointed out a possible poisoning effect also coming from CO₂, that appeared to be mostly reversible but important upon continuous p_{CO_2} [98]. On the other side, at the present state of the art, it appears to be hard to significantly compare data of LaNi₅ with CeNi₅ for the quite limited number of reports and investigations.

According to Yamagishi et al. and Jain et al. [31,99], CeNi₅ does not show a relevant H₂ adsorption in standard conditions, suggesting a limited dissociation and thus, in principle, a lower surface reconstruction upon interaction with H₂; thus, in this case, the decomposition of the intermetallic during catalytic test, could in principle arise by reaction with H₂O. At the present, data for CO₂ effects are not available, but will be further investigated in the future.

4. Conclusions

Several Ni-based intermetallics were prepared by arc-melting and tested as catalytic precursors in Sabatier's reaction and their performance was compared with that of commercial CO₂ hydrogenation catalysts provided by Clariant.

The following conclusions can be deduced from results discussed in the present work:

1. Commercial catalyst performance approaches forecasted thermodynamic equilibrium above 573 K achieving 100% yield to methane at 573 K and a GHSV of 55000 h⁻¹.
2. No catalytic activity has been observed for Al₉Co₂, Al₃Ni and Al₁₃Fe₄.
3. The catalytic performances of RENi₅ intermetallics appear to be a function of the chosen pretreatment and exposure to the reacting gas.
4. LaNi₅ is mainly active toward rWGS.
5. The best catalyst activity is achieved over CeNi₅ where the yield to CH₄ reaches 49% at 723 K upon reduction at 873 K for 4 h, even if this yield is lower than commercial catalyst.
6. Both RENi₅ exhaust catalysts were characterized by powder XRD and FE-SEM techniques and they are constituted by Ni particles supported over RE oxides with a mean size of about 10 nm. Thus, based on these results, promising material could be developed relying on possibly high surface IMCs.
7. Position-space chemical bonding analysis performed on both LaNi₅ and CeNi₅ reveals a charge transfer from the RE to the Ni species with the formation of polar interactions, as evidence by the ELI-D/QTAIM analysis. Both two- and four-atomic RE-Ni bonds are realized,

together with four-atomic Ni₄ interactions reminiscent of the bonding picture realized in the elemental face-centered cubic nickel.

8. The decomposition of the studied intermetallics under hydrogenation conditions was successfully investigated by surface simulations and chemical understanding on the basis of the ELI-D mapping approach. The suitable attack sites for H₂ molecules were not simply found in correspondence of the largest hole, but in surface regions corresponding to high ELI-D values, i.e. dangling bonds. The latter originates from uncompensated multi-atomic bonds that extend toward the vacuum space. Their interactions with H₂ lead to the dissociation of such molecules together with the formation of hydride anions, that penetrate in the subsurface region; at the same time, Ni atoms are oxidized to the metallic state and migrate toward the surface, supporting the experimentally detected formation of the catalytically active Ni(O).

CRedit authorship contribution statement

Riccardo Freccero: Conceptualization, Methodology, Software, Validation, Formal analysis, Investigation, Writing - Original Draft, Writing - Review & Editing, Visualization, Funding acquisition. **Elena Spennati:** Validation, Investigation, Resources, Writing - Original Draft, Writing - Review & Editing, Visualization. **Gabriella Garbarino:** Conceptualization, Methodology, Data Curation, Writing - Review & Editing, Supervision, Project administration, Funding acquisition. **Paola Riani:** Conceptualization, Methodology, Data Curation, Writing - Review & Editing, Supervision, Project administration, Funding acquisition.

Declaration of Competing Interest

The authors declare that they have no known competing financial interests or personal relationships that could have appeared to influence the work reported in this paper.

Data Availability

Data will be made available on request.

Acknowledgements

GG and PR acknowledge Clariant for providing commercial CO₂ hydrogenation catalyst. GG and ES acknowledge the Project funded under the National Recovery and Resilience Plan (NRRP), Mission 4 Component 2 Investment 1.3 - Call for tender No. 1561 of 11.10.2022 of Ministero dell'Università e della Ricerca (MUR); funded by the European Union - NextGenerationEU, PE0000021, "Network 4 Energy Sustainable Transition - NEST". RF acknowledges the University of Genoa for funding the "COMET - CO₂ METHanation through interMETallics" project through the "Curiosity Driven 2021" call, funded by the European Union - NextGenerationEU.

Appendix A. Supporting information

Supplementary data associated with this article can be found in the online version at [doi:10.1016/j.apcatb.2023.123532](https://doi.org/10.1016/j.apcatb.2023.123532).

References

- [1] (<https://joint-research-centre.ec.europa.eu>) (accessed 2022-23-27).
- [2] (<https://ukcop26.org/cop26-goals>) (accessed 2022-12-27).
- [3] A.I. Tsotsias, N.D. Charisiou, I.V. Yentekakis, M.A. Goula, Capture and methanation of CO₂ using dual-function materials (DFMs), Chem. Proc. 2 (2020) 35, <https://doi.org/https://doi.org/10.3390/ECCS2020-0756710.3390/ECCS2020-07567>.
- [4] Y. Wu, J. Lin, Y. Xu, G. Ma, J. Wang, M. Ding, Transition metals modified Ni-M (M=Fe, Co, Cr and Mn) catalysts supported on Al₂O₃-ZrO₂ for low-temperature

- CO₂ methanation, *ChemCatChem* 12 (2020) 3553–3559, <https://doi.org/10.1002/cctc.202000399>.
- [5] L. Li, W. Zeng, M. Song, X. Wu, G. Li, C. Hu, Research progress and reaction mechanism of CO₂ methanation over Ni-based catalysts at low temperature: a review, *Catalysts* 12 (2022) 244, <https://doi.org/10.3390/catal12020244>.
 - [6] E. Spennati, P. Riani, G. Garbarino, A perspective of lanthanide promoted Ni-catalysts for CO₂ hydrogenation to methane: catalytic activity and open challenges, *Catal. Today* 418 (2023), 114131, <https://doi.org/10.1016/j.cattod.2023.114131>.
 - [7] International Energy Agency (IEA), The Role of Critical World Energy Outlook Special Report Minerals in Clean Energy Transitions, 2022. (<https://iea.blob.core.windows.net/assets/fdd2a83b-8c30-4e9d-980a-52b6d9a86fdc/TheRoleofCriticalMineralsinCleanEnergyTransitions.pdf>) (accessed 2023–07–30).
 - [8] G.E.R. Schulze, *Metallphysik*, Akademie-Verlag, Berlin, 1967.
 - [9] M. Armbrüster, R. Schlögl, Yu Grin, Intermetallic compounds in heterogeneous catalysis – a quickly developing field, *Sci. Technol. Adv. Mater.* 15 (2014), 034803, <https://doi.org/10.1088/1468-6996/15/3/034803>.
 - [10] M. Armbrüster, Intermetallic compounds in catalysis – a versatile class of materials meets interesting challenges, *Sci. Technol. Adv. Mater.* 21 (2020) 303–322, <https://doi.org/10.1080/1080/14686996.2020.1758544>.
 - [11] M. Escudero-Escribano, P. Malacrida, M.H. Hansen, U.G. Vej-Hansen, A. Velazquez-Palenzuela, V. Tripkovic, J. Schiotz, J. Rossmeisl, I.E.L. Stephens, I. Chorkendorff, Tuning the Activity of Pt Alloy Electrocatalysts by Means of the Lanthanide Contraction, *Science* 352 (6281) (2016) 73–76, <https://doi.org/10.1126/science.aad8892>.
 - [12] S. Feng, Y. Geng, H. Liu, H. Li, Targeted Intermetallic Nanocatalysts for Sustainable Biomass and CO₂ Valorization, *ACS Catal.* 12 (2022) 14999–15020, <https://doi.org/10.1021/acscatal.2c03443>.
 - [13] S. Furukawa, T. Komatsu, Intermetallic Compounds: Promising Inorganic Materials for Well-Structured and Electronically Modified Reaction Environments for Efficient Catalysis, *ACS Catal.* 7 (2017) 735–765, <https://doi.org/10.1021/acscatal.6b02603>.
 - [14] M. Armbrüster, K. Kovnir, M. Friedrich, D. Teschner, G. Wowsnick, M. Hahne, P. Gille, L. Szentmiklósi, M. Feuerbacher, M. Heggen, F. Girgsdies, D. Rosenthal, R. Schlögl, Yu Grin, Al₁₃Fe₄ as a low-cost alternative for palladium in heterogeneous hydrogenation, *Nat. Mater.* 11 (2012) 690–693, <https://doi.org/10.1038/nmat3347>.
 - [15] R.R. Zimmermann, T. Hahn, W. Reschtilowski, M. Armbrüster, Kinetic Parameters for the Selective Hydrogenation of Acetylene on GaPd₂ and GaPd, *Chem. Phys. Chem.* 18 (2017) 2517–2525, <https://doi.org/10.1002/cphc.201700535>.
 - [16] N. Köpfle, L. Mayr, D. Schmidmair, J. Bernardi, A. Knop-Gericke, M. Hävecker, B. Klötzer, S. Penner, A comparative discussion of the catalytic activity and CO₂-Selectivity of Cu-Zr and Pd-Zr (intermetallic) compounds in methanol steam reforming, *Catalysts* 7 (2017) 53–69, <https://doi.org/10.3390/catal7020053>.
 - [17] R. Zerdoumi, O. Matselko, L. Röbner, B. Sarkar, Yu Grin, M. Armbrüster, Disentangling Electronic and Geometric Effects in Electrocatalysis through Substitution in Isostructural Intermetallic Compounds, *J. Am. Chem. Soc.* 144 (2022) 8379–8388, <https://doi.org/10.1021/jacs.2c03348>.
 - [18] H. Zhang, D. Mao, J. Zhang, D. Wu, Regulating the Crystal structure of Layered Double Hydroxide-Derived Co-In Catalysts for Highly Selective CO₂ Hydrogenation to Methanol, *Chem. Eng. J.* 452 (2023), 139144, <https://doi.org/10.1016/j.cej.2022.139144>.
 - [19] M.S. Duyar, A. Gallo, J.L. Snider, T.F. Jaramillo, Low-pressure methanol synthesis from CO₂ over metal-promoted Ni-Ga intermetallic catalysts, *J. CO₂ Util.* 39 (2020), 101151, <https://doi.org/10.1016/j.jcou.2020.03.001>.
 - [20] N.A.A. Rusman, M. Dahari, A review on the current progress of metal hydrides material for solid-state hydrogen storage applications, *Int. J. Hydrog. Energy* 41 (2016) 12108–12126, <https://doi.org/10.1016/j.ijhydene.2016.05.244>.
 - [21] R. Tsukuda, R. Yamagishi, S. Kameoka, C. Nishimura, A.-P. Tsai, Ability of hydrogen storage CeNi_{5-x}Ga_x and Mg₂Ni alloys to hydrogenate acetylene, *Sci. Technol. Adv. Mater.* 20 (2019) 774–785, <https://doi.org/10.1080/14686996.2019.1629836>.
 - [22] R. Tsukuda, T. Kojima, D. Okuyama, S. Kameoka, C. Nishimura, A.-P. Tsai, Hydrogenation of acetylene and propyne over hydrogen storage ErNi_{5-x}Al_x alloys and the role of absorbed hydrogen, *Int. J. Hydrog. Energy* 45 (2020) 19226–19236, <https://doi.org/10.1016/j.ijhydene.2020.05.062>.
 - [23] K. Soga, H. Imamura, S. Ikeda, Hydrogenation of ethylene over LaNi₅ alloy, *J. Phys. Chem.* 81 (1977) 1762–1766, <https://doi.org/10.1021/j100533a010>.
 - [24] R. Tsukuda, T. Kojima, Y. Xu, C. Nishimura, M. Krajčí, S. Kameoka, High Catalytic Activities of RENi_{5-x}Al_x (RE = La, Er) and Low Activity of Mg₂Ni Following Hydrogen Uptake: The Role of Absorbed Hydrogen, *J. Phys. Chem. C* 125 (2021) 20919–20929, <https://doi.org/10.1021/acs.jpcc.1c06484>.
 - [25] M. Lelis, S. Varnagiris, M. Urbanavicius, K. Zakarauskas, Investigation of Catalyst Development from Mg₂NiH₄ Hydride and Its Application for the CO₂ Methanation Reaction, *Coatings* 10 (2020) 1178, <https://doi.org/10.3390/coatings10121178>.
 - [26] H. Ando, M. Fujiwara, Y. Matsumura, H. Miyamura, H. Tanaka, Y. Souma, Methanation of carbon dioxide over LaNi₄X-type intermetallic compounds as catalyst precursor, *J. Alloy. Compds.* 223 (1995) 139–141, [https://doi.org/10.1016/0925-8388\(94\)01488-4](https://doi.org/10.1016/0925-8388(94)01488-4).
 - [27] S. Kato, A. Borgschulte, D. Ferri, M. Biemann, J.-C. Crivello, D. Wiedenmann, M. Parlinska-Wojtan, P. Rossbach, Y. Lu, A. Remhof, A. Züttel, CO₂ hydrogenation on a metal hydride surface, *Phys. Chem. Chem. Phys.* 14 (2012) 5518–5526, <https://doi.org/10.1039/c2cp23264b>.
 - [28] J.M. Joubert, V. Paul-Boncour, F. Cuevas, J. Zhang, M. Latroche, LaNi₅ related AB₅ compounds: structure, properties and applications, *J. Alloy. Compds.* 862 (2021), 158163, <https://doi.org/10.1016/j.jallcom.2020.158163>.
 - [29] K. Yatagai, Y. Shishido, R. Gemma, T. Boll, H.H. Uchida, K. Oguri, Mechanochemical CO₂ methanation over LaNi-based alloys, *Int. J. Hydrog. Energy* 45 (2020) 5264–5275, <https://doi.org/10.1016/j.ijhydene.2019.07.055>.
 - [30] D. Zhong, L. Ouyang, J. Liu, H. Wang, Y. Jia, M. Zhu, Metallic Ni nanocatalyst in situ formed from LaNi₅H₅ toward efficient CO₂ methanation, *Int. J. Hydrog. Energy* 44 (2019) 29068–29074, <https://doi.org/10.1016/j.ijhydene.2019.02.153>.
 - [31] R. Yamagishi, T. Kojima, S. Kameoka, D. Okuyama, T.J. Sato, C. Nishimura, A.-P. Tsai, Creating the hydrogen absorption capability of CeNi₅ through the addition of Al, *Int. J. Hydrog. En.* 42 (2007) 21832–21840, <https://doi.org/10.1016/j.ijhydene.2017.07.072>.
 - [32] G. Garbarino, P. Riani, L. Magistri, G. Busca, A study of the methanation of carbon dioxide on Ni/Al₂O₃ catalysts at atmospheric pressure, *Int. J. Hydrog. En.* 39 (2014) 11557–11565, <https://doi.org/10.1016/j.ijhydene.2014.05.111>.
 - [33] G. Garbarino, D. Bellotti, P. Riani, L. Magistri, G. Busca, Methanation of carbon dioxide on Ru/Al₂O₃ and Ni/Al₂O₃ catalysts at atmospheric pressure: Catalysts activation, behaviour and stability, *Int. J. Hydrog. En.* 40 (2015) 9171–9182, <https://doi.org/10.1016/j.ijhydene.2015.05.059>.
 - [34] G. Garbarino, C. Wang, T. Cavattoni, E. Finocchio, P. Riani, M. Flytzani-Stephanopoulos, G. Busca, A study of Ni/La-Al₂O₃ catalysts: A competitive system for CO₂ methanation, *Appl. Catal. B: Environ.* 248 (2019) 286–297, <https://doi.org/10.1016/j.apcatb.2018.12.063>.
 - [35] H. Verbeek, W.M.H. Sachtler, The study of the alloys of platinum and Tin by chemisorption, *J. Catal.* 42 (1976) 257–267, [https://doi.org/10.1016/0021-9517\(76\)90260-8](https://doi.org/10.1016/0021-9517(76)90260-8).
 - [36] X. Li, A. Scherf, M. Heilmair, F. Stein, The Al-Rich Part of the Fe-Al Phase Diagram, *J. Phase Equilibria Diffus.* 37 (2016) 162–173, <https://doi.org/10.1007/s11669-015-0446-7>.
 - [37] H. Okamoto, M.E. Schlesinger, E.M. Mueller, *ASM Handbook Vol. 3 Alloy Phase Diagrams*, ASM International, 1992. ISBN: 978-1-62708-070-5.
 - [38] W. Kraus, G. Nolze, POWDER CELL - a program for the representation and manipulation of crystal structures and calculation of the resulting X-ray powder patterns, *J. Appl. Crystallogr.* 29 (1996) 301–303, <https://doi.org/10.1107/S0021889895014920>.
 - [39] D. Schwarzenbach, *Program LATCON: Refine Lattice Parameters*, University of Lausanne, 1966.
 - [40] H. Putz, K. Brandenburg, Match! - Phase Analysis using Powder Diffraction, Crystal Impact, GbR, Kreuzherrenstr. 102, 53227 Bonn, Germany, (<https://www.crystallimpact.de/match>).
 - [41] P.M. De Wolff, J.W. Visser, Absolute intensities, Rep. 641.109 Technische Physische Dienst, Delft 1964, Netherlands.
 - [42] J.P. Perdew, K. Burke, M. Ernzerhof, Generalized Gradient Approximation Made Simple, *Phys. Rev. Lett.* 77 (1996) 3865, <https://doi.org/10.1103/PhysRevLett.77.3865>.
 - [43] K. Koepernik, H. Eschrig, Full-Potential Nonorthogonal Local-Orbital Minimum-Basis Band-Structure Scheme, *Phys. Rev. B* 59 (1999) 1743–1757, <https://doi.org/10.1103/PhysRevB.59.1743>.
 - [44] M. Juckel, P. Koželj, Y. Prots, A. Ormeci, U. Burkhardt, A. Leithe-Jasper, E. Svanidze, Intermediate Valence Behavior of Yb₂CuAl₈, *Z. für Anorg. und Allg. Chem.* 646 (2020) 1238–1243, <https://doi.org/10.1002/zaac.202000118>.
 - [45] S. Flipo, M. Kohout, F. Roth, T. Weigel, W. Schnelle, M. Bobnar, A. Ormeci, U. Burkhardt, C. Hennig, T. Leisegang, D.-C. Meyer, A. Leithe-Jasper, R. Gumenuik, CeMo₂Bs: A New Type of Arrangement of Puckered Boron Hexagonal Rings, *Eur. J. Inorg. Chem.* (31) (2019) 3572–3580, <https://doi.org/10.1002/ejic.201900411>.
 - [46] M. Kohout, A Measure of Electron Localizability, *Int. J. Quantum Chem.* 97 (2004) 651–658, <https://doi.org/10.1002/qua.10768>.
 - [47] F.R. Wagner, V. Bezugly, M. Kohout, Yu Grin, Charge Decomposition Analysis of the Electron Localizability Indicator: A Bridge between the Orbital and Direct Space Representation of the Chemical Bond, *Chem. – Eur. J.* 13 (2007) 5724–5741, <https://doi.org/10.1002/chem.200700013>.
 - [48] A. Ormeci, H. Rosner, F.R. Wagner, M. Kohout, Yu Grin, Electron Localization Function in Full-Potential Representation for Crystalline Materials, *J. Phys. Chem. A* 110 (2006) 1100–1105, <https://doi.org/10.1021/jp054727r>.
 - [49] R.F.W. Bader, *Atoms in Molecules – A Quantum Theory*, Oxford University Press, New York, 1990.
 - [50] M. Kohout, DGrid-4.6, Radebeul, Germany, 2014.
 - [51] M. Kohout, DGrid-5.0, Dresden, Germany, 2018.
 - [52] S. Raub, G. Jansen, A Quantitative Measure of Bond Polarity from the Electron Localization Function and the Theory of Atoms in Molecules, *Theor. Chem. Acc.* 106 (2001) 223–232, <https://doi.org/10.1007/S002140100268>.
 - [53] D. Bende, F.R. Wagner, Yu Grin, 8 - N Rule and Chemical Bonding in Main-Group MgAs-Type Compounds, *Inorg. Chem.* 54 (2015) 3970–3978, <https://doi.org/10.1021/acs.inorgchem.5b00135>.
 - [54] F.R. Wagner, D. Bende, Y. Grin, Heteropolar Bonding and a Position-Space Representation of the 8 - N Rule, *Dalton Trans.* 45 (2016) 3236–3243, <https://doi.org/10.1039/C5DT04140F>.
 - [55] R. Freccero, Yu Grin, W. Wagner, Polarity-extended 8 - N^{eff} rule for semiconducting main-group compounds with the TiNiSi-type of crystal structure, *Dalton Trans.* 52 (2023) 8222–8236, <https://doi.org/10.1039/D3DT00621B>.
 - [56] V. Blum, R. Gehrke, F. Hanke, P. Havu, V. Havu, X. Ren, K. Reuter, M. Scheffler, Ab initio molecular simulations with numeric atom-centered orbitals, *Comput. Phys. Commun.* 180 (2009) 2175–2196, <https://doi.org/10.1016/j.cpc.2009.06.022>.
 - [57] E. Van Lenthe, E.J. Baerends, J.G. Snijders, Relativistic total energy using regular approximations, *J. Chem. Phys.* 101 (1994) 9783–9792, <https://doi.org/10.1063/1.467943>.
 - [58] A. Baranov, *Vis. Plugin ParaView* (2015).

- [59] U. Ayachit, The ParaView Guide: A Parallel Visualization Application, Kitware (2015).
- [60] P. Villars, K. Cenzual, Pearson's Crystal Data: Crystal Structure Database for Inorganic Compounds (Release), ASM International, Materials Park, Ohio, USA, 2021/22.
- [61] R. Ferro, A. Saccone, *Intermetallic Chemistry*, Elsevier Pergamon Material Series, 2008.
- [62] R.G. Barnes, W.C. Harper, S.O. Nelson, D.K. Thome, D.R. Torgeson, Investigation of systems LaNi_5H_x and LaNi_5D_x by proton and deuteron nuclear magnetic resonance, *J. Less Common Met.* 49 (1976) 483–502, [https://doi.org/10.1016/0022-5088\(76\)90060-6](https://doi.org/10.1016/0022-5088(76)90060-6).
- [63] T.P. Blach, E.M. Gray, Magnetic properties of the $\text{LaNi}_5\text{-H}$ system, *J. Alloy. Compd.* 253 (1997) 336–338, [https://doi.org/10.1016/S0925-8388\(96\)02916-7](https://doi.org/10.1016/S0925-8388(96)02916-7).
- [64] A.F. Al Alam, S.F. Matar, M. Nakhil, N. Ouafni, Investigation of changes in crystal and electronic structures by hydrogen within LaNi_5 from first-principles, *Solid State Sci.* 11 (2009) 1098–1106, <https://doi.org/10.1016/j.solidstatesciences.2009.02.026>.
- [65] T. Ito, H. Ido, Electronic structures and magnetic properties of LaCo_5 , LaNi_5 , and LaCo_2Ni_2 , *J. Appl. Phys.* 97 (2005), 10A313, <https://doi.org/10.1063/1.1854280>.
- [66] A. Jain, S.P. Ong, G. Hautier, W. Chen, W.D. Richards, S. Dacek, S. Cholia, D. Gunter, D. Skinner, G. Ceder, K.A. Persson, Commentary: The Materials Project: A materials genome approach to accelerating materials innovation, *APL Mater.* 1 (2013), 011002, <https://doi.org/10.1063/1.4812323>. Data for LaNi_5 (mp-2317) and CeNi_5 (mp-1910).
- [67] H. Zheng, S. Lin, First-principles calculation of LaNi_5 surface, *J. Phys.: Conf. Ser.* 29 (2006) 129, <https://doi.org/10.1088/1742-6596/29/1/025>.
- [68] M. Gupta, Electronic properties of LaNi_5 and LaNi_5H_7 , *J. Less Common Met.* 130 (1987) 219–227, [https://doi.org/10.1016/0022-5088\(87\)90113-5](https://doi.org/10.1016/0022-5088(87)90113-5).
- [69] G.E. Grechnev, A.V. Logosha, A.S. Panfilov, A.G. Kuchin, A.N. Vasilev, Effect of pressure on the magnetic properties of YNi_5 , LaNi_5 , and CeNi_5 , *Low. Temp. Phys.* 37 (2011) 138–143, <https://doi.org/10.1063/1.3555874>.
- [70] H. Mizoguchi, S.-W. Park, H. Hosono, A View on Formation Gap in Transition Metal Hydrides and Its Collapse, *J. Am. Chem. Soc.* 143 (2021) 11345–11348, <https://doi.org/10.1021/jacs.1c06307>.
- [71] L. Agnarelli, Y. Prots, U. Burkhardt, M. Schmidt, P. Kozelj, A. Leithe-Jasper, Yu Grin, Mg_3Pt_2 : Anionic Chains in a Eu_3Ga_2 -Type Structure, *Inorg. Chem.* 60 (2021) 13681–13690, <https://doi.org/10.1021/acs.inorgchem.1c01995>.
- [72] R. Freccero, P. Solokha, S. De Negri, A. Saccone, Yu Grin, F.R. Wager, Polar-Covalent Bonding Beyond the Zintl Picture in Intermetallic Rare-Earth Germanides, *Chem. Eur. J.* 25 (2019) 6600–6612, <https://doi.org/10.1002/chem.201900510>.
- [73] R. Freccero, S. De Negri, A. Saccone, P. Solokha, Solid state interactions in the La-Au-Mg system: phase equilibria and chemical bonding, *Dalton Trans.* 49 (2020) 12056–12067, <https://doi.org/10.1039/D0DT02359K>.
- [74] R. Freccero, S. De Negri, G. Rogl, G. Binder, H. Michor, P.F. Rogl, A. Saccone, P. Solokha, $\text{La}_2\text{Pd}_3\text{Ge}_5$ and $\text{Nd}_2\text{Pd}_3\text{Ge}_5$ Compounds: Chemical Bonding and Physical Properties, *Inorg. Chem.* 60 (2021) 3345–3354, <https://doi.org/10.1021/acs.inorgchem.0c03744>.
- [75] R. Freccero, P. Solokha, S. De Negri, Unpredicted but It Exists: Trigonal Sc_2Ru with a Significant Metal–Metal Charge Transfer, *Inorg. Chem.* 60 (2021) 10084–10088, <https://doi.org/10.1021/acs.inorgchem.1c01168>.
- [76] A. Amon, E. Svanidze, A. Ormeci, M. König, D. Kasinathan, D. Takegami, Y. Prots, Y.-F. Liao, K.-D. Tsuei, L.H. Tjeng, A. Leithe-Jasper, Yu Grin, Interplay of Atomic Interactions in the Intermetallic Semiconductor Be_5Pt , *Angew. Chem. Int. Ed.* 58 (2019) 15928–159293, <https://doi.org/10.1002/anie.201909782>.
- [77] Y. Gong, J. Wu, M. Kitano, J. Wang, T.-N. Ye, J. Li, Y. Kobayashi, K. Kishida, H. Abe, Y. Niwa, H. Yang, T. Tada, H. Hosono, Ternary intermetallic LaCoSi as a catalyst for N_2 activation, *Nat. Catal.* 1 (2018) 178–185, <https://doi.org/10.1038/s41929-017-0022-0>.
- [78] A.M. Barrios Jiménez, A. Ormeci, S.G. Altendorf, F. Kaiser, U. Burkhardt, I. Veremchuk, G. Auffermann, Yu Grin, Intermetallic compounds M_2Pt ($\text{M} = \text{Al, Ga, In, Sn}$) in the oxygen evolution reaction, *Sustain. Energy Fuels* 5 (2021) 5762, <https://doi.org/10.1039/D1SE01190A>.
- [79] I. Antonyshyn, O. Sichevych, A. Ormeci, U. Burkhardt, K. Rasim, S. Titlbach, M. Armbrüster, S.A. Schunk, Yu Grin, Ca-Ag compounds in ethylene epoxidation reaction, *Sci. Technol. Adv. Mater.* 20 (2019) 904, <https://doi.org/10.1080/14686996.2019.1655664>.
- [80] D.A. Lang, J.V. Zaikina, D.D. Lovingood, T.E. Gedris, S.E. Latturmer, $\text{Ca}_2\text{LiC}_3\text{H}$: A New Complex Carbide Hydride Phase Grown in Metal Flux, *J. Am. Chem. Soc.* 132 (2010) 17523–17530, <https://doi.org/10.1021/ja107436n>.
- [81] S.F. Matar, Intermetallic hydrides: A review with ab initio aspects, *Prog. Solid State Chem.* 38 (2010) 1–37, <https://doi.org/10.1016/j.progsolidstchem.2010.08.003>.
- [82] X.-J. Feng, Y. Prots, M. Bobnar, M.P. Schmidt, W. Schnelle, J.-T. Zhao, Yu Grin, Zintl-Phase $\text{Sr}_3\text{LiAs}_2\text{H}$: Crystal Structure and Chemical Bonding Analysis by the Electron Localizability Approach, *Chem. Eur. J.* 21 (2015) 14471–14477, <https://doi.org/10.1002/chem.201501236>.
- [83] C. Lartigue, A. Percheron-Guégan, J.-C. Achard, F. Tasset, Thermodynamic and structural properties of $\text{LaNi}_{5-x}\text{Mn}_x$ compounds and their related hydrides, *J. Less Common Met.* 173 (1980) 23–29, [https://doi.org/10.1016/0022-5088\(80\)90365-3](https://doi.org/10.1016/0022-5088(80)90365-3).
- [84] A. Amon, A. Ormeci, M. Bobnar, L.G. Akselrud, M. Avdeev, R. Gumeniuk, U. Burkhardt, Y. Prots, C. Hennig, A. Leithe-Jasper, Yu Grin, Cluster Formation in the Superconducting Complex Intermetallic Compound $\text{Be}_{21}\text{Pt}_5$, *Acc. Chem. Res.* 51 (2018) 214–222, <https://doi.org/10.1021/acs.accounts.7b00561>.
- [85] L. Agnarelli, Y. Prots, M. Schmidt, M. Knel, E. Svanidze, U. Burkhardt, A. Leithe-Jasper, Yu Grin, Be_3Ru : Polar Multiatomic Bonding in the Closest Packing of Atoms, *ChemistryOpen* 11 (2022), e202200118, <https://doi.org/10.1002/open.202200118>.
- [86] R. Freccero, P. Solokha, D.M. Proserpio, A. Saccone, S. De Negri, A new glance on R_2MGe_6 ($\text{R} = \text{rare earth metal, M} = \text{another metal}$) compounds. An experimental and theoretical study of R_2PdGe_6 germanides, *Dalton Trans.* 46 (2017) 14021–14033, <https://doi.org/10.1039/C7DT02686B>.
- [87] R. Freccero, L.C.J. Pereira, P. Solokha, S. De Negri, Flux Growth, Crystal Structure, and Chemical Bonding of Yb_2PdGe_3 , an AlB_2 Superstructure within the Rare-Earth Series, *Inorg. Chem.* 62 (2003) 1988–1999, <https://doi.org/10.1021/acs.inorgchem.2c03303>.
- [88] A. Martinelli, D. Ryan, J. Sereni, C. Ritter, A. Leineweber, I. Curlik, R. Freccero, M. Giovannini, Magnetic phase separation in the EuPdSn_2 ground state, *J. Mater. Chem. C* 11 (2023) 7641–7653, <https://doi.org/10.1039/D3TC00764B>.
- [89] S. Penner, P.D. Kheyrollahi Nezhad, Steering the Catalytic Properties of Intermetallic Compounds and Alloys in Reforming Reactions by Controlled in Situ Decomposition and Self-Activation, *ACS Catal.* 11 (2021) 5271–5286, <https://doi.org/10.1021/acscatal.1c00718>.
- [90] S. Han, X.-B. Zhang, S.-Q. Shi, M. Kohyama, H. Tanaka, N. Kuriyama, N. Taoka, T. Kaneko, Q. Xu, CO Adsorption on a LaNi_5 Hydrogen Storage Alloy Surface: A Theoretical Investigation, *ChemPhysChem* 9 (2008) 1564–1569, <https://doi.org/10.1002/cphc.200800080>.
- [91] Z. Łodziańska, Surface Properties of LaNi_5 and TiFe – Future Opportunities of Theoretical Research in Hydrides, *Front. Energy Res.* 9 (2021), 719375, <https://doi.org/10.3389/fenrg.2021.719375>.
- [92] S.A. Villaseca, A. Ormeci, S.V. Levchenko, R. Schlögl, Yu Grin, M. Armbrüster, CO Adsorption on GaPd —Unravelling the Chemical Bonding in Real Space, *ChemPhysChem* 18 (2017) 334–337, <https://doi.org/10.1002/cphc.201601162>.
- [93] B. Li, C. Xiao, N.M. Harrison, R.M. Fogarty, A.P. Horsfield, Role of electron localisation in H adsorption and hydride formation in the Mg basal plane under aqueous corrosion: a first-principles study, *Phys. Chem. Chem. Phys.* 25 (2023) 5989–6001, <https://doi.org/10.1039/D2CP05242C>.
- [94] P. Riani, I. Valsamakis, T. Cavattoni, V. Sanchez Escibano, G. Busca, G. Garbarino, $\text{Ni/SiO}_2\text{-Al}_2\text{O}_3$ catalysts for CO_2 methanation: Effect of SiO_2 addition, *Appl. Catal. B: Environ.* 284 (2021), 119697, <https://doi.org/10.1016/j.apcatb.2020.119697>.
- [95] P. Riani, E. Spennati, M. Villa Garcia, V. Sanchez Escibano, G. Busca, G. Garbarino, $\text{Ni/Al}_2\text{O}_3$ catalysts for CO_2 methanation: Effect of silica and nickel loading, *Int. J. Hydrog. Energy* 48 (2023) 24976–24995, <https://doi.org/10.1016/j.ijhydene.2023.01.002>.
- [96] T.P. Blach, E.M. Gray, Magnetic properties of the $\text{LaNi}_5\text{-H}$ system, *J. Alloy. Compd.* 253 (1997) 336–338, [https://doi.org/10.1016/S0925-8388\(96\)02916-7](https://doi.org/10.1016/S0925-8388(96)02916-7).
- [97] K.H.J. Buschow, Hydrogen adsorption in intermetallic compounds, in: K. A. Gschneidner Jr, L. Roy Eyring (Eds.), *Handbook on the Physics and Chemistry of Rare Earths*, Volume 6, Elsevier, 1984, pp. 1–112.
- [98] N. Hanada, T. Nakagawa, H. Asada, M. Ishida, K. Takahashi, S. Isobe, I. Saita, K. Asano, Y. Nakamura, A. Fujisawa, S. Miura, Dependence of constituent elements of AB_5 type metal hydrides on hydrogenation degradation by CO_2 poisoning, *J. Alloy. Compd.* 647 (2015) 198–203, <https://doi.org/10.1016/j.jallcom.2015.05.253>.
- [99] R.K. Jain, A. Jain, S. Agarwal, N.P. Lalla, V. Ganesan, D.M. Phase, I.P. Jain, Hydrogenation behaviour of Ce-based AB_5 intermetallic compounds, *J. Alloy. Compd.* 440 (2007) 84–88, <https://doi.org/10.1016/j.jallcom.2006.08.326>.